agronomy

Article

Organic Matter and Mineral Composition of Silicate Soils: FTIR Comparison Study by Photoacoustic, Diffuse Reflectance, and Attenuated Total Reflection Modalities

Dmitry S. Volkov [1,2], **Olga B. Rogova** [2] and **Mikhail A. Proskurnin** [1,*]

[1] Chemistry Department, M.V. Lomonosov Moscow State University, Leninskie Gory, 1-3, GSP-1, 119991 Moscow, Russia; dmsvolkov@gmail.com
[2] Department of Chemistry and Physical Chemistry of Soils, V.V. Dokuchaev Soil Science Institute, Pyzhevsky per., 7/2, 119017 Moscow, Russia; obrogova@gmail.com
* Correspondence: proskurnin@gmail.com

Abstract: This study aims to compare photoacoustic (FTIR–PAS), diffuse reflectance (DRIFT), and attenuated total reflection (ATR) FTIR modalities in the wide wavenumber range from NIR (7500 cm^{-1}) to FIR (150 cm^{-1}) for the same silicate soil samples under the same conditions. The possibilities of non-destructive rapid qualitative analysis of soils by these modalities without comprehensive data treatment were compared. The assignment of more than 100 bands for the chernozem and sod-podzolic as common types of silicate types of soil was made. The following groups of bands of organic matter and inorganic matrix were reliably found in spectra of all or at least two modalities: 3690–3680 cm^{-1} (hydrogen-bonded SiO–H . . . H_2O stretch, not ATR), 2930–2910 cm^{-1} and 2860–2850 cm^{-1} (methylene stretch), 1390–1380 cm^{-1}, (symmetric stretch carboxylate, DRIFT and FTIR–PAS); 2000–1990 cm^{-1}, 1885 cm^{-1}, and 1790–1783 cm^{-1} (SiO_2 overtones, DRIFT and FTIR–PAS), 1163–1153 cm^{-1}, SiO_2 lattice (not FTIR–PAS), 1037 cm^{-1} (Si–O or Al–O stretch), 796 cm^{-1} (lattice symmetrical Si–O–Si stretch); 697 cm^{-1}, SiO_2; and 256 cm^{-1} (not FTIR–PAS). Amide I, II, and III bands appear in DRIFT and FTIR–PAS spectra while not in ATR. Except for methylene and carboxylate groups, CH vibrations (3100–2900 cm^{-1}) are not seen in ATR. Bands at 1640–1630 cm^{-1}, 1620–1610 cm^{-1}, 1600–1598 cm^{-1} (primary water bands and probably carboxylate) appear in the spectra of all three modalities but are unresolved and require data treatment. It is preferable to use all three modalities to characterize both soil organic matter and mineral composition. DRIFT provides the maximum number of bands in all three modalities and should be selected as a primary technique in the NIR and 4000–2000 cm^{-1} regions for hydrogen-bonding bands, CH_X groups, and the silicate matrix. ATR–FTIR complements DRIFT and provides a good sensitivity for soil water and the matrix in 2000–400 cm^{-1}. FTIR–PAS in 4000–1500 cm^{-1} reveals more bands than DRIFT and shows the highest sensitivity for absorption bands that do not appear in DRIFT or ATR-IR spectra. Thus, FTIR–PAS is expedient for supporting either DRIFT or ATR–FTIR. This modality comparison can be a basis for methodological support of IR spectroscopy of soils and similar organomineral complexes.

Keywords: soil composition; soil organic matter; soil mineral composition; chernozem; sod-podzolic soil; diffuse reflectance IR spectroscopy; attenuated total internal reflection IR spectroscopy; photoacoustic IR spectroscopy

check for updates

Citation: Volkov, D.S.; Rogova, O.B.; Proskurnin, M.A. Organic Matter and Mineral Composition of Silicate Soils: FTIR Comparison Study by Photoacoustic, Diffuse Reflectance, and Attenuated Total Reflection Modalities. *Agronomy* **2021**, *11*, 1879. https://doi.org/10.3390/agronomy11091879

Academic Editors: Evgeny Lodygin and Elena Shamrikova

Received: 24 August 2021
Accepted: 17 September 2021
Published: 19 September 2021

1. Introduction

Soil changes, including formation, degradation, the outcome of agricultural use, anthropogenesis, remediation, and environmental impacts, require an increasing volume and quality of information [1,2]. Apart from bulk physical and physicochemical soil properties as the largest solid carbon reservoir [3–5], a new challenge is the composition and structures of soil microaggregates and fractions [6–9]. The central problem of soil assessment is soil organic matter (SOM) as an organomineral continuum of high- and low-molecular organic and inorganic substances in a finely dispersed state [10–12].

All these problems necessitate highly informative methods of analysis and monitoring. However, most chemical analysis methods for SOM do not always provide complete information, for instance, for such relevant factors as mineral–organic interactions, and involve extensive sample preparation, altering soil properties. More information with less impact on the original soil and SOM composition can be obtained with non-destructive, highly informative molecular spectroscopy methods of IR spectroscopy [13,14]. The position of IR spectroscopy in soil studies constantly expands due to a new technological level, advances in instrumental capabilities, new modalities, and increased inherent sensitivity [15–19].

The applications of IR spectroscopy for soils are widespread and primarily oriented to humic substances [20–25], the total SOM or soil organic carbon [26,27], the texture and mineralogy of clay minerals and their organomineral complexes [28,29], or the availability of artificial additions such as nutrients or fertilizers [30,31]. In addition, IR spectroscopy is used to evaluate fertility, structuration, or biological activity of soils, as well as organomineral complexes, taking IR spectra as indicators of these properties [26–29,32]. Soil identification by its IR spectra has been developed [31,33–37]. However, this complex task has not yet been solved completely, especially from the viewpoint of the use of several modalities of IR spectroscopy.

Considering IR modalities, transmission IR spectroscopy with pressed KBr-matrix sample tablets is the first-born, simplest, and still most widespread modality [38,39]. However, it requires milling in nonaqueous solvents, which, along with not fully chemically inert tablet matrix, may lead to significant chemical composition distortion and structural changes [40,41]. Therefore, IR spectroscopy in soil analysis is based on other modalities [18,34,42,43]. First, diffuse reflection IR Fourier-transform (DRIFT) spectroscopy is widely used to analyze and assess soils and organomineral complexes [18,19,26,28,43–47]. However, the soil particle size profoundly impacts DRIFT spectra, as the size dispersion and particle distribution affect the reflection and may result in high measurement errors [45,48], even for the same types of soil samples.

Attenuated-total reflection IR spectroscopy (ATR–FTIR) is the second most widespread method for soils. It is used for both SOM contents [49–51] and its constituents [18,52–55], adsorbed water and minerals [19,56], and artificial soil components [57,58]. It is advantageous from the viewpoint of sample preparation and technical implementation for various types of soil samples. However, apart from changing the properties upon clamping dry samples, the soil may not provide good contact with the ATR crystal, resulting in sensitivity and precision loss; meanwhile, wetting may also distort the measurement [59].

Interferometer-based FTIR photoacoustic spectroscopy (FTIR–PAS) is the third modality widespread in soil and SOM IR analysis [1,30,53,60–65]. It is different from the two above reflection modalities and transmission modalities because not the transmitted or reflected radiation after the interaction with the sample is measured, but the heat waves caused by sample absorption. Thus, this modality can be considered an alternative to transmission, DRIFT, or ATR techniques and is less dependent on the particle size. This method is a developed instrument for complex samples [53,66–73]. It is used for mineral, polymer, and technological samples, modeling the dependence of soil properties on its physical and elemental composition, moisture, porosity, and density [31,37,61,73–78]. FTIR–PAS provides many well-defined bands and a broader region of the informational spectrum [31,79]. Most widespread FTIR–PAS soil applications include identifying components (mainly mineral matrices such as carbonate, silicate, and clay minerals; SOM; or fertilizers) and researching plants and other objects [2,33,37,62,63]. The possibilities of FTIR–PAS for assessing the distribution of a substance over the depth of microparticles were considered for model particles [80] and soils [53].

Therefore, all three modalities have their specific features, and the selection of the modality depends on several—from fundamental to practical—aspects. Comparing various modalities for complex samples such as biochars or soils has recently been reflected in reviews or feature papers [32,52,81]. However, as far as we are concerned, a complete comparison of features of all three modalities—DRIFT, ATR–FTIR, and FTIR–PAS—for soils was not made previously. Thus, additional studies of all IR modalities from the viewpoint of the applicability and volume of information are of demand.

Thus, this study aims to compare three modalities of FTIR spectroscopy (DRIFT, ATR–FTIR, and FTIR–PAS) in the wide wavenumber range from NIR (7500 cm^{-1}) to FIR (150 cm^{-1}) for the same soil samples under the same conditions. Within this study frame, we compared primarily qualitative data with the estimation of the potential of some quantitative measurements by these modalities to compare the sensitivity and information contents and select the modalities for various tasks. We selected sod-podzolic and chernozem as widespread soil types with the silicate matrix and SOM composition, which are different due to the formation conditions.

2. Materials and Methods

2.1. Soils

We used two silicate matrix soil types, sod-podzolic and chernozems, due to the differences in the organic matter composition caused by the contrast in the conditions of their formation: climatic, hydrological, lithological, vegetation cover, and microbiological activity. For the latter, we used samples with different agricultural use.

2.1.1. Sod-Podzolic Soil

Samples were taken on the experimental field of the Zelenograd station of the V.V. Dokuchaev Soil Institute (village of Eldigino, Moscow region, Russia), operating since 1964. Since 2011, the field has not been plowed; a fallow has formed (*Sonchus arvensis*, *Festuca pratensis*, *Phleum pratense*, *Dactylis glomerata*). Samples were taken in 2016; the sampling site coordinates are 56°07′56″ N 37°48′09″ E (Figure S1, Supplementary Materials). The soil is agrosod-podzolic medium loamy (sod-podzolic, Umbric Albeluvisols Abruptic (WRB 2006), Eutric Podzoluvisols (FAO)) formed on a mantle loam, underlain at a depth of 2–3 m with non-carbonate moraine. The content of silt fraction of ≤ 1 μm is 15–16% [82]. Minerals with a rigid structure dominate the mineralogical composition of the clay fraction (hydromica, chlorite-vermiculites, kaolinite, chlorites in the upper part). The content of clay minerals with a rigid structure is 85–82%, with a labile (swelling) structure (mica-smectites, chlorite-smectites) of 15–18% [83]. Larger fractions are dominated by quartz, potassium feldspars, plagioclases, micas. Organic carbon content, 1.37% *w/w*; pH 5.96.

2.1.2. Chernozem Soils

Typical chernozems (heavy loamy) of the Kursk region (Russia) with a significantly different history and intensity of agricultural use were sampled: native (intact, annually mown) steppe vegetation, permanent bare fallow since 1964, shelterbelt since 1964, arable cropland under wheat, cultivated without crop rotation since 1964 [84]. Samples were taken on the territory of the long-term field experiment of the Kursk Research Institute of Agricultural Production and V.V. Alekhin Tsentralno-Chernozemny Nature Reserve of Russia [85], Figures S2 and S3 of the Supplementary Materials. The granulometric composition is heavy silty-clay loam. Main components: quartz, 35–40%; illites, 12–15%; smectites, 12–15%; and total organic carbon, 4–6%. The humus horizon (A + AB1) is 105–130 cm. Soil boiling after the addition of 10% HCl begins at a depth of 65–70 cm. The arable layer bulk density (0–30 cm) ranges from 1.20 to 1.25 g/cm^3 [86].

General soil samples with a mass of 2 kg were taken at the end of May 2017 from sections 1.5 m deep along genetic horizons and additionally with a step of 10 cm. For this study, the topsoil layer, 0–10 cm, was taken. General samples were dried for two weeks in air, then stored at room temperature. An average 0.5 kg sample was taken from the corresponding total sample, and separated into aggregate fractions by dry sieving.

The annually mown native steppe site is covered with natural steppe vegetation on V.V. Alekhin Tsentralno-Chernozemny Nature Reserve of Russia; it is a sample of intact typical chernozem. Samples were taken from the section with coordinates 51°34′13.6″ N 36°05′23.1″ E. The vegetation cover is approximately 100% *Bromus riparius L.*, *Festuca sulcata Hack.*, *Galium verum L.*, *Salvia pratensis L.*, *Iris pumila L.*, *Adonis vernalis L.*, *Vicia tenuifolia Roth.*, *Stipa pennata*, *Stipa pulcherrima*, and *Stipa tirsa*. Organic carbon content, 5.79% *w/w*; pH 6.55.

Permanent bare fallow since 1964 is a plot bordering on a plot of the annually mown steppe, where the soil is processed annually, plowing without sowing and fertilizers. Thus, since 1964, fresh organic matter almost did not get into this type of soil. Soil samples were taken in the center of the plot, at ca. 50 m from the section on the native steppe sampling site. Organic carbon content, 2.80% *w/w*; pH 6.0.

On the territory of the long-term field experiment of the Kursk Scientific Research Institute of Agricultural Production, soil samples were taken from the protective shelterbelt (51°37′17.1″ N 36°15′42.0″ E), established in 1964. The forest shelterbelt, limiting the experimental fields, forms a variant of the soil, which structure is restored under the influence of forest vegetation and which, compared with the arable chernozem lands, shows a decent structure [87]. Currently, it is a dead-cover forest without a live grass layer, approx. 60 years old. Forest-forming species: *Quercus robur*, *Fraxinus excelsior*, *Acer campestre*. Organic carbon content, 4.75% *w/w*, pH 6.1.

Arable soil is under permanent wheat 51°37′17.1″ N 36°15′42.0″ E with annually applied mineral fertilizers since 1964; organic carbon content, 3.55% *w/w*; pH 7.3.

Dry fractionation of averaged samples was carried out on an AS 200 sieving machine (Retsch GmbH, Haan, Germany) with a dry sieving holder and a set of precision sieves with a stainless steel mesh, 200 mm in diameter, and square mesh sizes of 50, 63, 71, 80, 90, 100, 250, and 500 µm, and 1, 2, and 5 mm (Retsch GmbH). Ultramicro sieves with a diameter of 200 mm and square cells of 20, 30, and 40 µm (Precision Eforming LLC, Cortland, NY, USA) were used to obtain fine fractions. The dry sieving procedure consisted of sieving the whole sample (ca. 300 g) on a 5000, 2000, 1000, 500, 250, 100, and 50 µm sieve column. Then, a fraction of 50–100 µm (ca. 10–30 g) was processed on a column with 90, 80, 71, and 63 µm sieves. The obtained fraction below 50 µm (ca. 1–20 g) was sieved through a 40, 30, and 20 µm sieves column. The sieving time on each of the three stages was 15 min (paused for a short time each minute) at a sieving amplitude of 3 mm. Thus, soil fractions with particle sizes below 20, 20–30, 30–40, 40–50, 50–63, 63–71, 71–80, 80–90, 90–100, 100–250, 250–500, 500–1000, 1000–2000, 2000–5000, and above 5000 µm were obtained.

2.2. Instrumentation

IR spectra were recorded on a single-beam IR Fourier spectrometer, Bruker Vertex 70 (Bruker Optik GmbH, Ettlingen, Germany) with a KBr beam splitter or a wide-range Si beam splitter and a wide-range room-temperature DLaTGS detector or liquid-nitrogen-cooled photovoltaic MCT detector. The spectrometer, accessories, and attachments were continuously purged with a flow of 500 L/h of dry air (–70 °C dew point, a PG28L Purge Gas Generator, PEAK Scientific, Glasgow, United Kingdom). The laboratory temperature was maintained at 23 ± 1 °C using an air conditioner. All spectra were processed by OPUS 7.5 software (Bruker Optik GmbH, Ettlingen, Germany). DRIFT and ATR–FTIR spectra were smoothed out by 13 points; FTIR–PAS, by 25 points [88,89] (at some figures, spectra are presented without smoothing). Smoothed spectra did not show a shift of the band maxima upon smoothing.

2.2.1. DRIFT

A PrayingMantis^{TM} diffuse reflection accessory (Harrick Scientific Products, Inc., Pleasantville, NY, USA) was used (Table S1, Supplementary Materials). The software automatically converted spectra measured in diffuse reflectance using the Kubelka–Munk (*KM*) conversion $KM = (1 - Refl)^2/2Refl$, *Refl* is the ratio of reflected and incident light. Absorbance spectra are converted to transmittance. The smallest value allowed for transmittance or reflectance is 0.001%, which equals a Kubelka–Munk value of ca. 500.

For background measurements, the tilted alignment mirror for the PrayingMantis^{TM} accessory was used. The alignment fixture was slid into the accessory, the horizontal mirror going in first. In this orientation, the tilted mirror is in the sampling position.

2.2.2. ATR–FTIR

A GladiATR^{TM} single reflection attenuated total internal reflection accessory with a diamond crystal (Pike Technologies, Madison, WI, USA) was used (Table S2, Supplementary Materials). A background signal was recorded before each new sample. The soil spectra were recorded using a wide-range silicon beam splitter in the range of wavenumbers of 4000–100 cm^{-1}; the baseline was not corrected. The ATR–FTIR spectra were additionally transformed as $I_0 a + b = I_{corr}$, where I_0 is the ATR–FTIR intensity after the operations above, I_{corr} is the ATR–FTIR intensity compared to the FTIR–PAS spectra, $a = 150$, $b = 1$.

2.2.3. FTIR–PAS

FTIR–PAS spectra were obtained using an MTEC PAC300 photoacoustic accessory (MTEC Photoacoustic, Inc., Ames, IA, USA), Table S3, Supplementary Materials, by varying the interferometer modulation frequency (IMF); software correction of CO_2 and H_2O bands was not used. Samples were placed in a cell installed in the accessory, and the cell compartment was purged with helium for 5–10 s. The background signal spectrum was recorded using highly pure compressed graphite before each image. Samples weight, 5–10 mg. For IMF of 1.6 and 2.5 kHz, sample signal amplification modes were 1000 and 2000 times, respectively; the intensity was multiplied by $\sqrt{\widetilde{v}}$ [89].

3. Results

In all the test samples of chernozem and sod-podzolic soils, matrix minerals are composed mainly of quartz species, hydrosilicate minerals—illites and smectites—and clay minerals with the due percentage of amorphous silicon dioxide or hydrosilicate species [82,83,85,90–95]. Due to the complexity of samples and many (although sometimes non-detailed) assignments in the literature, we summed up all the possible entries in an assignment table (Table 1), giving both counterparts of target bands, inorganic matrix components, and SOM constituents. The comparison and differences in spectra for specific IR modalities are given in the following sections. The spectra for the studied soils are shown in Figure 1 for DRIFT, Figure 2 for ATR–FTIR, and Figure 3 for FTIR–PAS, and Figure S4 (Supplementary Materials) for different modalities. This section describes the assignment of all major bands reliably present in at least two of three modalities or most relevant bands characteristic for a single modality only.

Table 1. Band assignments for silicate-based soils (chernozem and agrosod-podzolic soils and size fractions).

#	Band, cm^{-1}	Quartz/Silicate/Si–O Constituents, Water, Inorganic Constituents	Organic Constituents	DRIFT	ATR–FTIR	FTIR–PAS
	7400	(?) Water vapor	1st overtone C–H stretch + C–H deformation (in hemicelluloses and lignin [96]	medium	n/a	n/a
	7100	OH stretch, the first overtone [97]	(2ν + δ) CH$_2$ [28]	strong	n/a	n/a
	6000	—	CH$_3$ stretch, the first overtone [28] or combination band, the first overtone Aryl–H stretch [96]	weak	n/a	absent
	5800–5750	—	CH$_2$ stretch, the first overtone [98]	weak	n/a	absent
	5250	Water combination band $\upsilon_2 + \upsilon_3$	—	strong	n/a	weak
	4900	The first overtone CO$_2$	—	weak	n/a	absent
	4740	—	CH + OH, cellulose	weak	n/a	absent
	4630	The first overtone CO$_2$	CH + OH, cellulose	weak, shoulder	n/a	absent
	4530	Water combination band OH ν + δ [28]	—	strong	n/a	very weak, noisy
	4440	—	CH combination (ν + δ) [28]	medium	n/a	absent
	4330	—	CH combination $(\nu + \delta)_{as}$ [28] or C–O stretch + O–H stretch or C–H$_2$ bend. + C–H$_2$ stretch Cellulose [96]	medium	n/a	absent
	4260	—	CH combination $(\nu + \delta)_s$ [28], cellulose [96]	medium	n/a	absent
	4180	—	CH combination, lignin [96]	weak	n/a	absent
	4010–3970	Hydrogen-bonded SiOH . . . HOSi SiO–H stretch (kaolinite, clay) O–H stretch isolated (?)	CH, a combination or overtone band [99] C–O stretch + C–H and C–H$_2$ stretch (cellulose) [96]	strong, broad	absent	very weak
	3740–3730	Hydrogen-bonded SiOH . . . HOSi SiO–H stretch (kaolinite, clay) O–H stretch isolated CO$_2$	—	absent	absent	medium to weak
	3700	Unbonded SiO–H stretch, tilted (kaolinite, clay) [100]	—	weak, shoulder, unresolved	absent	weak, shoulder, unresolved
	3690–3680	Hydrogen-bonded SiO–H . . . H$_2$O stretch (amorphous) [100]	—	strong	weak	medium
	3670–3650	OH stretching of inner-surface hydroxyl groups, anti-phase vibration with transition moment lying in the (001) plane of kaolinite [101,102]	—	weak	absent	medium

Table 1. *Cont.*

#	Band, cm^{-1}	Quartz/Silicate/Si–O Constituents, Water, Inorganic Constituents	Organic Constituents	DRIFT	ATR–FTIR	FTIR–PAS
	3640–3630	Isolated SiO–H OH stretch (α-quartz) [100]	—	weak	absent	medium
	3620	Isolated (inner) SiO–H [101,102] OH stretch (α-quartz) [100] Al(Mg)SiO–H stretch, straight	—	strong	weak	strong
	3540–3500	Hydrogen-bonded SiO–H . . . H_2O SiO–H stretch (amorphous) [100]	—	absent	absent	weak
	3490	Liquid water: antisynchronous stretch v_3	O–H, phenolic, alcohol, carboxylic	strong, broad, unresolved	strong unresolved	strong, broad
	3270	Liquid water: synchronous stretch, v_1	O–H, phenolic, alcohol, carboxylic C = O overtone			strong, broad
	3220	N–H stretch	—	absent	absent	weak
	3180	OH stretch intramolecular [103]	—	absent	absent	weak
	3130–3110	—	C–H aromatic chains stretch	absent	absent	weak
	3070–3065	—	C–H aromatic chains stretch	very weak, shoulder	absent	weak
	3030–3035	—	C–H aromatic chains stretch C–H alkene chains stretch	very weak	absent	weak
	3000–2995	—	C–H aromatic chains stretch C–H alkene chains stretch	absent	absent	weak
	2970–2960	(?) SiO_2 overtone, complex overtone-combination bands [104–106]	C–H, CH_3 antisymmetric stretch [28]	weak	absent	medium to weak
	2930–2910	(?) SiO_2 overtone, complex overtone-combination bands [104–106]	C–H, CH_2 antisymmetric stretch [35,70,107,108]	strong	medium to weak, broad	strong
	2880	—	C–H, CH_3 symmetric stretch [28]	weak	absent	weak
	2860–2850	—	C–H, CH_2 symmetric stretch [35,70,107,108]	strong	medium to weak, broad	medium
	2360, 2340	CO_2 [109]	—	very weak to absent	absent	medium
	2260–2220	SiO_2 overtone ≅2×1095	—	medium to weak	negative, artifact	medium to weak
	2140	SiO_2 overtone ≅2 × 1070 Water: combination of v_2 + libration	—	weak	negative, artifact	weak
	2030	SiO_2 combination band ≅1000 + 1037	Overtone, C–H aromatic bend (?)	medium	absent	medium, shoulder
	2000–1990	SiO_2 overtone ≅2 × 1000	C=O stretch	medium, unresolved	negative, artifact	medium
	1975	SiO_2 combination band ≅920 + 1037 or 970 + 1000 [104]	C=O stretch		negative, artifact	medium

Table 1. *Cont.*

#	Band, cm^{-1}	Quartz/Silicate/Si–O Constituents, Water, Inorganic Constituents	Organic Constituents	DRIFT	ATR–FTIR	FTIR–PAS
	1950–1945	(?) SiO_2 combination band $\cong$960 + 1000	C=O stretch	medium	absent	medium
	1885	(?) SiO_2 overtone $\cong$2 × 975	C=O stretch	strong, shoulder	weak	strong, shoulder
	1865	(?) SiO_2 combination band $\cong$697 + 1163	C=O stretch	strong	weak	strong
	1820	—	C=O stretch, the anhydride of carboxyl groups	very weak, shoulder	absent	weak, shoulder
	1790–1783	(?) SiO_2 Combination band $\cong$800 + 1000	C=O stretch	strong	weak	strong
	1775	—	C=O stretch	shoulder	absent	medium
	1730–1720	—	C=O stretch	weak	medium	medium
	1710–1680	(?) SiO_2 combination band $\cong$697 + 1000	N–H bend, amine Alkene –C=C– stretch, substituted aromatics	strong shoulder unresolved	medium to weak shoulder	strong shoulder unresolved
	1650–1640	Absorbed liquid water bend v_2, [110]	Amide I, aromatic –C=C– stretch [26,78]		strong, unresolved	
	1620–1610	HO–H stretch [100] Liquid: bend (v_2) of the covalent bonds Hydrogen-bonded SiOH . . . H_2O	N–H bend, C=O stretch	strong		strong
	1600–1598	(?) SiO_2 overtone $\cong$2 × 796 Vapor: bend (v_2) of the covalent bonds	C–C stretch, aromatic rings	strong shoulder	strong, unresolved	strong shoulder
	1580	—	Antisymmetric stretch carboxylate NH_2 [28]	medium shoulder	medium shoulder	medium shoulder
	1570–1560	—	(?) C–C stretch Aromatic rings	weak shoulder (x)	very weak	medium, artefact (carbon black)
	1540–1520	SiO_2 combination band 450 + 1070 [111]	Amide II, aromatic rings, carboxyl C	medium to strong	weak shoulder	medium
	1460	(?) Amorphous SiO_2 combination band $\cong$350 + 1153 Carbonate [47]	O–H, C–H scissoring [29]	weak shoulder, unresolved	weak	medium
	1440	—	Carboxyl C–O–H in-plane bend [112]	absent	weak, shoulder	medium to weak
	1420	Mg–OH stretch [104]	C–O stretch	weak, shoulder, unresolved	medium, broad	medium to weak
	1390–1380	SiO_2 Amorphous or SiO_2 overtone $\cong$2 × 697 Combination band $\cong$350 + 1000 [104] O–H (coordinated bonded water)	Symmetric stretch carboxylate a combination band of phenolic or COO stretch vibrations with CH_2 and CH_3 bands Non-carboxyl C–O–H in-plane bend [113]	strong, unresolved	absent	strong

Table 1. *Cont.*

#	Band, cm^{-1}	Quartz/Silicate/Si–O Constituents, Water, Inorganic Constituents	Organic Constituents	DRIFT	ATR–FTIR	FTIR–PAS
	1340	—	CH$_2$ wagging	strong, unresolved	absent	weak
	1320–1310	—	In-phase CH$_2$ twisting [28]	strong, unresolved	weak shoulder	weak shoulder
	1285–1280	SiO$_2$ Combination band ≅450 + 795	Amide III, C–O stretch of aromatic rings and carboxylic acids [108], C–O stretch CH$_2$ rocking C–N stretch	strong to medium, shoulder, unresolved	medium shoulder	medium shoulder
	1235	Silicates Combination band SiO$_2$ ≅470 + 760; Lattice [106]	Amide III, C–O stretch of aromatic rings and carboxylic acids	strong to medium, shoulder, unresolved	absent	medium, shoulder
	1185	Amorphous silica [114]Combination band SiO$_2$ [104]	CH$_2$ wagging	weak, shoulder	absent	medium, shoulder
	1165–1153	SiO$_2$ lattice [106]	C–OH stretching of aliphatic O–H [115]	strong	medium	weak shoulder
	1115–1105	Amorphous silica [116]	Mon-carboxyl C–O stretch	weak	broad medium	broad medium,
	1095	SiO$_2$ silicate Si–O stretch [114] P–O [117]	In-plane C–H bend (non-aromatic) and cellulose (?)	weak		
	1080–1075	O–Si–O lattice stretch [106]	C–N [28]	absent	very weak	weak
	1037	Silicate (kaolinite, illite) Si–O tetrahedra stretch Asymmetrical stretch Al–O stretch [26,47] P–O [117]	In-plane C–H bend (non-aromatic) and (?) carbohydrates	strong, shoulder	strong, shoulder	strong, shoulder
	1010–995	SiO$_2$ Si–O stretch lattice	—	weak broad	strong	strong, shoulder
	975	SiO$_2$ silicate (kaolinite, illite) Si–O stretch [114] Ti–O (Noda)	—	strong broad	strong shoulder	weak, shoulder
	930–910	Silicate, aluminosilicate [28], OH deformation of inner hydroxyl groups [102] Overtone ≅2 × 450 [114]	Carboxyl out-of-plane C–O–H bend	medium to weak, shoulder	strong, shoulder	strong, shoulder
	875	Si–O$^-$or Si–O–Si bridge [118] carbonate, calcite [101,118–121]	Aromatic bend, polyaromatic [26,122]	weak to absent	weak, shoulder	weak shoulder
	860	Al–OH (clay minerals)	—	very weak to absent	weak, shoulder	medium, shoulder
	840–830	Al–OH (clay minerals), smectite, and illite [123], AlMgOH [28]	Cellulose	medium shoulder (820)	absent	weak shoulder

Table 1. *Cont.*

#	Band, cm^{-1}	Quartz/Silicate/Si–O Constituents, Water, Inorganic Constituents	Organic Constituents	DRIFT	ATR–FTIR	FTIR–PAS
	813	Amorphous silica [116] Ti–O [124]	—	strong	absent	medium shoulder
	796	SiO$_2$ silicate Lattice symmetrical Si–O–Si stretch [106,114] (?) Overtone 2 × 395	Out-of-plane (oop) C–H bend (non-aromatic)	strong	strong	Strong, unresolved
	774	α-quartz Si–O–Si [106,116] Mg–OH, Al–OH (clay minerals)	—	strong	strong	
	750	Si–O, perpendicular [102] Mg–OH, Al–OH (clay minerals)	Polyaromatic compounds [122]	weak	weak	weak shoulder
	715	Water librations	Out of plane (oop) C–H bend (aromatic) In-phase rock vibrations of C_{4+} alkanes [28,125]	absent	weak	medium
	697–696	SiO$_2$ Si–O–Si bend [106]	—	strong	strong	strong
	675–670	CO$_2$ [126]	Out of plane (oop) C–H bend (aromatic)	medium to weak, shoulder	medium, shoulder	medium to weak, shoulder
	655–650	Silicate Si–O–Si bend, amorphous iron oxide	—	medium	weak shoulder	very weak
	645–640	Water librations Si–O [102] Sulfate [124]	Bentonite [35]	absent	weak	medium
	630–620	Ca$_3$-OH, hydroxyapatite [117]	C–S stretch [127]	medium	weak shoulder	weak shoulder
	620–610	CO$_2$	Non-carboxyl out-of-plane C–O–H bend	artifact	negative, artifact	weak shoulder
	565	PO$_4$ tetrahedra [117]	—	medium	absent	weak to absent
	535–525	α-quartz (?)* [106] Si–O–A1 deformation in kaolinite [102,128] Iron oxide [129]	—	absent	weak	medium
	517–513	Silicate O–Si–O bend [106]	—	medium	weak unresolved	medium
	505	(?) α-quartz [130]	—	absent		weak to absent
	490	SiO$_2$ O–Si–O bend [106]	—	absent	strong shoulder	medium

Table 1. *Cont.*

#	Band, cm^{-1}	Quartz/Silicate/Si–O Constituents, Water, Inorganic Constituents	Organic Constituents	DRIFT	ATR–FTIR	FTIR–PAS
	470	SiO_2 O–Si–O bend [114] O–Al–O [47]Iron oxide [129]	—	absent	strong	strong
	450	SiO_2 O–Si–O bend lattice [106,114]	—	weak shoulder unresolved	strong unresolved	medium to weak
	430–420	Si–O deformation of kaolinite [102] Mg-OH, Al–OH (clay minerals)	C–C in-phase vibrations [131]			medium
	402–392	SiO_2 O–Si–O bend lattice [106] water librations	—	strong	strong	strong
	375–370	$R(SiO_4)$ [104]; Amorphous silica [114]	—	absent	medium. shoulder	medium, shoulder
	360–355	SiO_2 Lattice	—	Strong	strong	medium
	350	(?) SiO_2 Lattice		absent	weak shoulder	weak shoulder
	330	(?) Mg–O stretch [104] Iron oxide [129]	—	very weak, shoulder	strong	medium
	275	Chlorides Ti-O [124]		weak shoulder	medium to weak	n/a
	263–260	α-Quartz [116]	—	strong	strong	n/a
	190–185	(?) α-Quartz		weak	weak	n/a
	130	α-Quartz, silica chlorides	—	medium	weak	n/a
	116–110	α-Quartz, silica	—	weak to absent	medium, noisy	n/a

Note: Color code: blue, a signature band (probably, available as an internal standard); green, reliable band; yellow, secondary band or should be used with caution; orange, the band cannot be used without data treatment and/or sample preparation; red, unusable or artifact band.

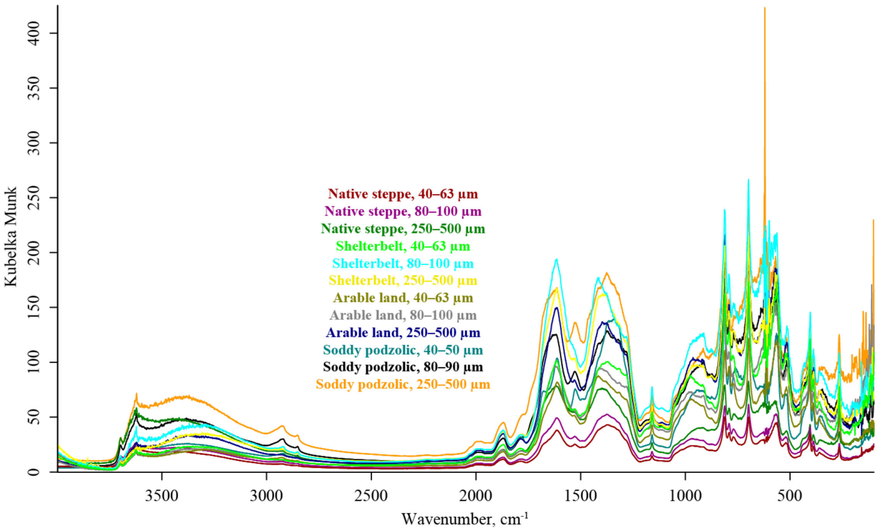

Figure 1. DRIFT spectra of fractions of chernozem and sod-podzolic soils. Chernozem native steppe, 40–63 µm, dark red; 80–100 µm, magenta; 250–500 µm, dark green; chernozem shelterbelt, 40–63 µm, light green; 80–100 µm, light blue; 250–500 µm, yellow; chernozem arable land, 40–63 µm, khaki; 80–100 µm, gray; 250–500 µm, dark blue; sod-podzolic, 40–50 µm, dark cyan; 80–90 µm, black; 250–500 µm, orange.

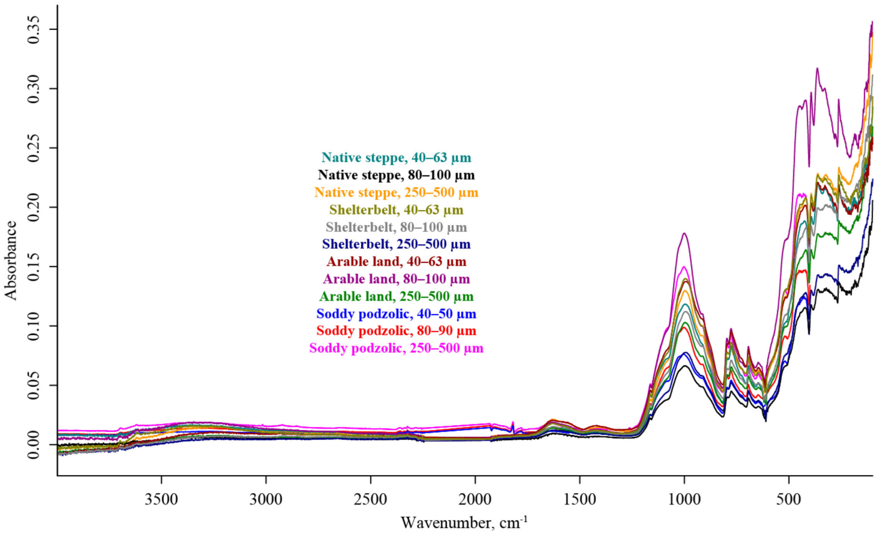

Figure 2. ATR–FTIR spectra of fractions of chernozem and sod-podzolic soils. Chernozem native steppe, 40–63 µm, dark cyan; 80–100 µm, black; 250–500 µm, orange; chernozem shelterbelt, 40–63 µm, khaki; 80–100 µm, gray; 250–500 µm, dark blue; chernozem arable land, 40–63 µm, dark red; 80–100 µm, dark magenta; 250–500 µm, dark green; sod-podzolic, 40–50 µm, blue; 80–90 µm, red; 250–500 µm, light magenta.

For all the studied samples, spectra in all modalities show good precision of the replicate portions of the same sample, and high reproducibility of spectra of replicate measurements of the same sample was achieved: the relative standard deviation was as low as 0.05–0.07 for the region of 4000–1000 cm^{-1}. In ATR–FTIR, the region 2500–2000 cm^{-1} suffers an increase in the noise level due to diamond crystal absorption and low radiation penetration depths. The region 2400–2300 cm^{-1} always shows the artifact peaks of gaseous CO_2, compensated by the software. Due to the high noise level and low signal intensities, ATR–IR spectra in 7500–4100 cm^{-1} and FTIR–PAS spectra in 300–100 cm^{-1} were not measured (denoted as "n/a" in Table 1). FTIR–PAS spectra depend on the IMF, which was considered previously; thus, we consider the FTIR–PAS modality at IMFs of 1.6 and 2.5 kHz, the spectra have the same relative intensity ratios.

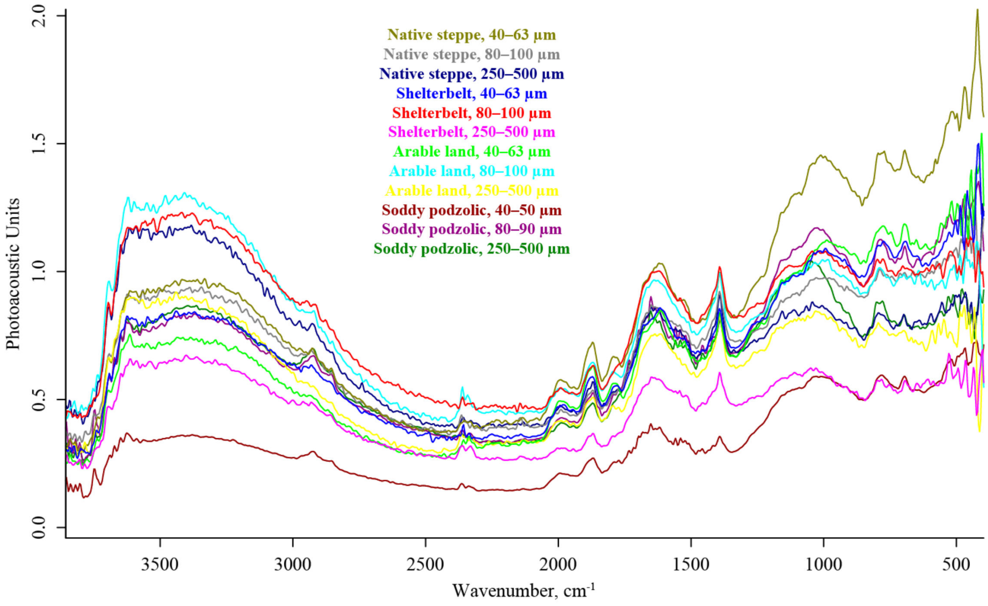

Figure 3. FTIR–PAS spectra (IMF, 1.6 kHz) of fractions of chernozem and sod-podzolic soils. Chernozem native steppe, 40–63 µm, khaki; 80–100 µm, gray; 250–500 µm, dark blue; chernozem shelterbelt, 40–63 µm, blue; 80–100 µm, red; 250–500 µm, light magenta; chernozem arable land, 40–63 µm, light green; 80–100 µm, light blue; 250–500 µm, yellow; sod-podzolic, 40–50 µm, dark red; 80–90 µm, dark magenta; 250–500 µm, dark green.

Due to a broad range of wavelengths, dividing the whole region into subregions was expedient. NIR region 7500–4000 cm^{-1} was considered separately as the overtone region 7500–5700 cm^{-1} and the combination region 5700–5700 cm^{-1}. The whole studied mid-IR and FIR range, 4000–150 cm^{-1}, was divided into six regions to divide inorganic components and organic matter. Namely, these regions are hydrogen-speciation region (4000–3100 cm^{-1}), CH region (3100–2800 cm^{-1}), quartz combination region (2800–1700 cm^{-1}), SOM region (1700–1170 cm^{-1}), quartz overtone region (1170–800 cm^{-1}), and quartz lattice region (800–150 cm^{-1}). These regions contain the dominating type of SOM or matrix bands and are readily and reproducibly dividable in the same manner for all the similar samples, both mineral and organic (e.g., humic substances). However, some provisional boundaries (e.g., 1170 and 1700 cm^{-1}) are reliable.

3.1. NIR Region (7500–4000 cm^{-1})

In the overtone region, 7500–5700 cm^{-1}, DRIFT provides a strong, broad first overtone OH stretch band [97] and several weak bands attributed to C–H bands [28,96,98]. ATR–FTIR and FTIR–PAS do not show any bands (Figure 4). FTIR–PAS spectra of all the modalities for wavenumbers higher than 7500 cm^{-1} are too noisy due to the low signal-to-noise ratio to make any conclusions.

More bands are revealed in the combination region 5700–4000 cm^{-1}. Here, DRIFT, in accordance with the previous studies [28,29], shows distinct, medium-intensity bands of water (5250 and 4530 cm^{-1}), CO_2 (the first overtone bands at 4900 and 4630 cm^{-1}), and bands that can be attributed to CH or combined CH/OH bands of cellulose and lignin fragments of SOM) [96]. FTIR–PAS in this region shows weak water combination bands only, although these bands are not suitable for further processing due to a low signal-to-noise ratio. Thus, DRIFT is the only modality for IR soil analysis in this region.

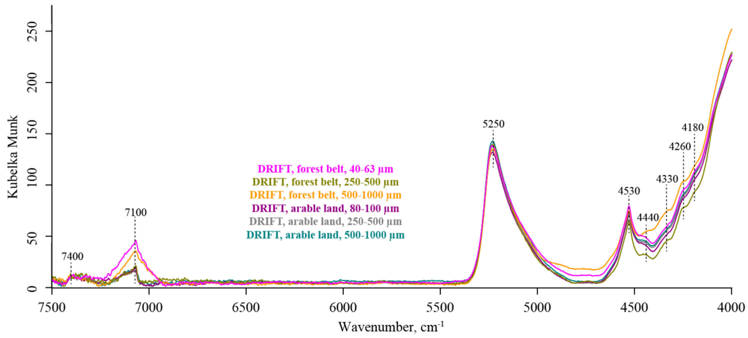

Figure 4. Normalized and scattering baseline-corrected DRIFT FTIR spectra in the region 7500–4500 cm^{-1} of chernozem soil (dry fractionation): forest belt, fractions, 40–63 µm, light magenta, 250–500 µm, khaki, and 500–1000 µm, orange; arable land, 80–100 µm, dark magenta, 250–500 µm, gray, and 500–1000 µm, dark cyan.

The only band that cannot be assigned reliably is the narrow band (weak in FTIR–PAS and strong in DRIFT) at 4010–3970 cm^{-1} that can be attributed both to overtone band of CH [99] or hydrogen-bonded bands represented by a series of bands with lower wavenumbers of a combination.

3.2. *Hydrogen-Speciation Region (4000–3100 cm^{-1})*

O–H stretching vibration continuum at 3700–3100 cm^{-1}, mainly from adsorbed water (Figure 5), dominates the hydrogen-speciation region (4000–3100 cm^{-1}). This broadband is deconvoluted into two matching contributions centered at 3490 and 3260 cm^{-1} from asynchronous and synchronous stretching vibrations of water [110]. In ATR–FTIR, they are unresolved, while DRIFT and sometimes FTIR–PAS show both maxima.

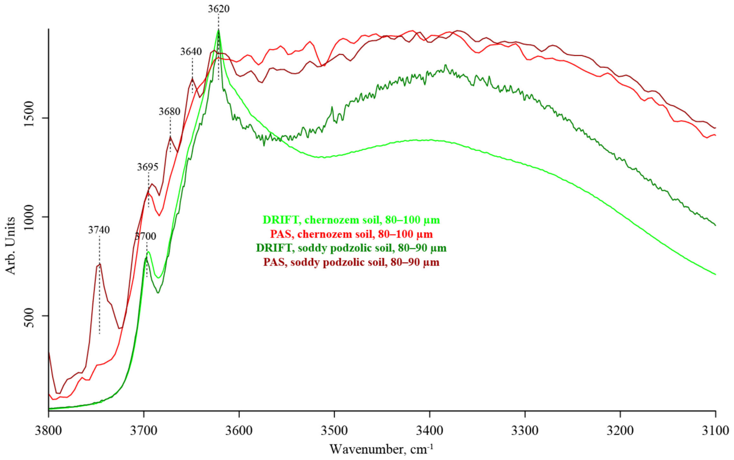

Figure 5. Normalized FTIR spectra in 3800–3100 cm^{-1}. DRIFT and PAS (IMF, 1.6 kHz) spectra of shelterbelt chernozem soil (dry fractionation, 80–100 µm), light green and light red, respectively; and DRIFT and PAS (IMF, 1.6 kHz) spectra of sod-podzolic soil (dry fractionation, 80–90 µm), dark green and dark red, respectively.

DRIFT shows a more reliable picture for two dominating intense bands at 3700–3690 cm^{-1} (hydrogen-bonded SiO–H . . . H_2O stretch (amorphous) [100]) and 3620 cm^{-1} (isolated or inner SiO–H [101,102]). These bands are almost undistinguishable in ATR–FTIR spectra. FTIR–PAS provides the most detailed picture, compared to DRIFT with an additional series of medium-to-strong sharp bands at 3730–3630 cm^{-1} attributed to metal-bonded O–H in clay minerals [77] and illites and smectites, 3730, 3700, 3670, and 3640–3630 cm^{-1} [123]. Another band at 3540–3500 cm^{-1} is absent in all the cases in DRIFT and ATR–FTIR modalities and relatively weak in FTIR–PAS, and can manifest hydrogen-bonded SiO–H . . . H_2O in amorphous species [100].

3.3. CH Region (3100–2800 cm^{-1})

On the shortwave shoulder of the broad OH continuum broadband, two peaks of C–H methylene stretching vibrations at 2930 cm^{-1} (asymmetric) and 2840 cm^{-1} (symmetric) [35,70,107,108] are seen in all three modalities; they are medium in ATR–FTIR and strong in FTIR–PAS and DRIFT (Figure 6). Following previous studies [52], these peaks are seen in slow-scan modes of FTIR–PAS and almost disappear in rapid-scan IMF modes at 7.5 kHz or higher. The peak shapes make it possible to exclude the contributions from vibrations of amorphous SiO_2 and quartz species [104–106]. Methyl group vibrations at 2880 cm^{-1} and 2970 cm^{-1} are absent in ATR–FTIR, weak in DRIFT, and distinct in FTIR–PAS. The relative intensities of methyl and methylene groups do not depend on the modality but are different for soil types. The region 3150–3030 cm^{-1} attributed to aromatic and alkane bands is manifested in FTIR–PAS only as a series of reproducible but weak bands.

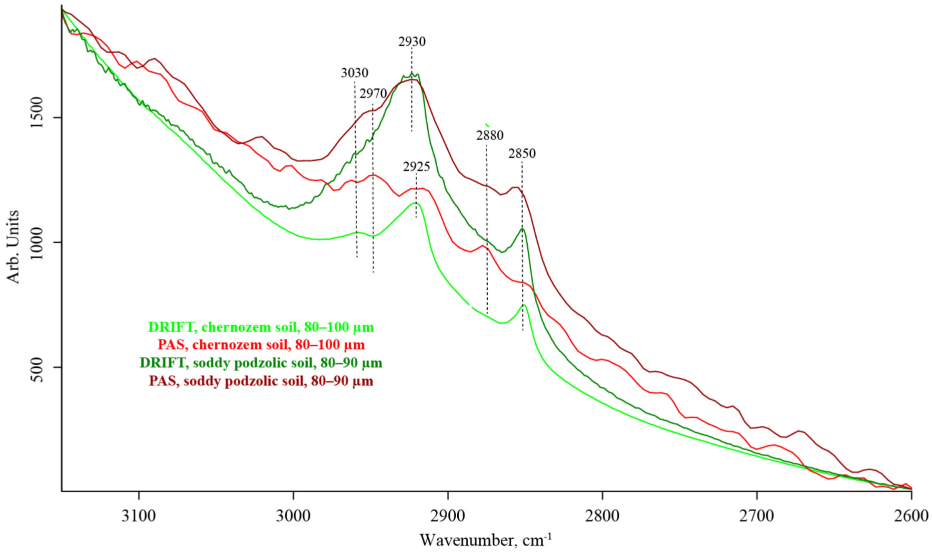

Figure 6. Normalized FTIR spectra in 3150–2700 cm^{-1}. DRIFT and PAS (IMF 1.6 kHz) spectra of shelterbelt chernozem soil (dry fractionation, 80–100 µm), light green and light red, respectively; and DRIFT and PAS (IMF 1.6 kHz) spectra of sod-podzolic soil (dry fractionation, 80–90 µm), dark green and dark red, respectively.

3.4. Quartz Combination Region (2800–1700 cm^{-1})

The subregion 2800–2000 cm^{-1} does not show any peaks except for the adsorbed CO_2 doublet (2360 and 2340 cm^{-1}); atmospheric CO_2 peaks are not considered and compensated by the software for DRIFT and ATR–FTIR. Low-intensity peaks at 2230 (broad, doublet) and 2140 cm^{-1} could be assigned to the second overtone and the combination of SiO_2 vibrations of 1153 and 1070 cm^{-1} [104,106]. They are manifested in FTIR–PAS only (Figure 7).

The region 2000–1750 cm^{-1} is dominated by overtone and combination bands of SiO_2; in this region, FTIR–PAS shows the largest volume of information, with DRIFT a close second; FTIR–PAS modality here is relatively meaningless. As previously shown [52], all the samples (except for silt fractions) show a very characteristic triplet of well-defined, intense, and nearly overlapping peaks at 1990, 1865 (the highest intensity), and 1790 cm^{-1} [47,104,105]. Relative intensities of this triplet do not change for all the studied samples and do not differ for DRIFT and FTIR–PAS modalities, and can be used as a signature of silicate soils and as an internal standard [52]. The same is valid for accompanying bands at 1945 and 1885 cm^{-1}, which may be the manifestation of nearly equal quartz and illite/smectite contributions [52,123].

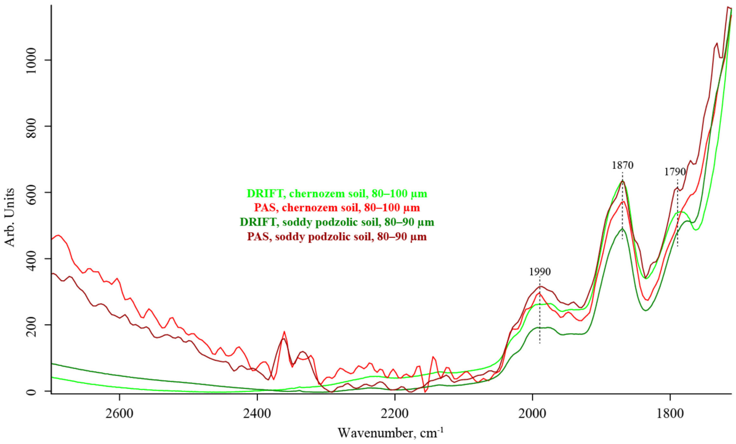

Figure 7. Normalized FTIR spectra in 2700–1700 cm^{-1}. DRIFT and PAS (IMF 1.6 kHz) spectra of shelterbelt chernozem soil (dry fractionation, 80–100 µm), light green and light red, respectively; and DRIFT and PAS (IMF 1.6 kHz) spectra of sod-podzolic soil (dry fractionation, 80–90 µm), dark green and dark red, respectively.

On the contrary, the bands at 1975, 1820, 1775, and 1730 cm^{-1} have different intensity for soil fractions and soil types and could be assigned to C=O stretching vibrations of various oxidized moieties of SOM, mainly carboxylic acids, and are consistent with the data from isolated humic substances [41,132]. These well-defined overtones and combination bands of silicate matrix are also manifestations of the saturation effects at the primary lattice vibrations of SiO$_2$ in DRIFT and FTIR–PAS modalities. Annealing experiments [52] do not show a change in the parameters of these bands, so it can be concluded that SOM contributions to these bands are negligible; thus, they can be recommended as internal standards for SOM studies as they depend on inorganic constituents only.

3.5. SOM Region (1700–1170 cm^{-1})

From the viewpoint of SOM analysis, the region 1700–1170 cm^{-1} is considered as a whole, but we separate it into two subregions, 1700–1450 and 1450–1170 cm^{-1}. Due to specific features of spectra in both subregions, the lower boundary is shifted to lower wavenumbers to consider the possible contribution of CH vibrations along with other SOM bands (Figure 8).

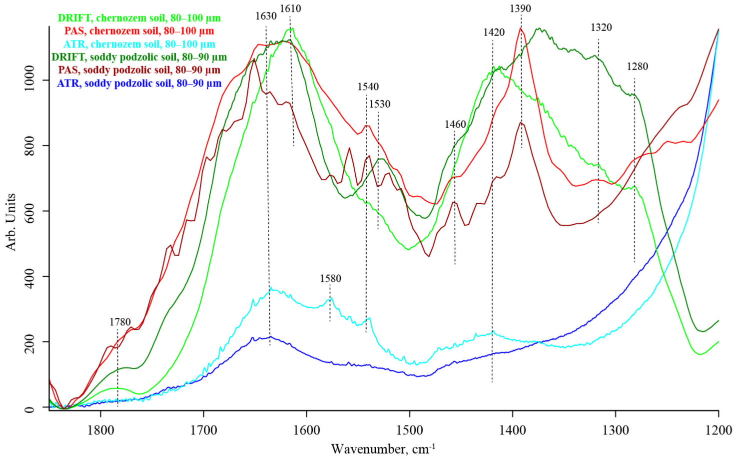

Figure 8. Normalized FTIR spectra in the region 1850–1200 cm^{-1}. DRIFT, ATR, and PAS (IMF, 1.6 kHz) spectra of shelterbelt chernozem soil (dry fractionation, 80–100 µm), light green, light blue, and light red, respectively; and DRIFT, ATR, and PAS (IMF, 1.6 kHz) spectra of sod-podzolic soil (dry fractionation, 80–90 µm), dark green, dark blue, and dark red, respectively.

Another reason is the usability of the modalities. Both DRIFT and FTIR–PAS are usable in this region, while ATR–FTIR still shows much less potential due to lower intensities and lower signal-to-noise ratios. The region of 1700–1450 cm^{-1} has the maximum number of overlapped bands with maximum counterparts in inorganic and SOM constituents. Relatively narrow bands can be found (in some fractions, by deconvolution) in 1710–1680 cm^{-1} and 1650–1640 cm^{-1} of the shortwave shoulder of the dominating broad water peak centered at 1615 cm^{-1}. These bands can be assigned to the C=C stretching of aromatic components of SOM [35] and have no distinct counterparts of inorganic matrix components. As we previously found for chernozem fractions and FTIR–PAS [52], the intensities of these bands for DRIFT and FTIR–PAS modalities are low. Thus, no quantitative approaches without sample preparation or data treatment were possible.

The broadband at 1670–1580 cm^{-1} is soil water [70]. The band is centered at 1620–1615 cm^{-1} and combines two peaks at 1650–1640 and 1600 cm^{-1} corresponding to the primary bending vibrations of absorbed water [110] and one of the essential overtone bands in quartz and silica (Table 1), respectively. The band components have different intensities: the bands are less resolved in DRIFT and FTIR–PAS, while the band at 1600 cm^{-1} is more pronounced in ATR–FTIR. All the modalities here experience a series of bands (mostly positive for DRIFT and ATR–FTIR and negative in FTIR–PAS), which appear due to gaseous water in the sample. Thus, these bands cannot be removed by instrument and sample compartment purging, which degrades the information quality in this region. The shoulder band at 1580 cm^{-1} has an equal intensity in all three modalities and corresponds to the carboxylate antisymmetric vibrations. Contrary to humic substances, this band in soils cannot be estimated with band deconvolution.

The long-wave shoulder of the 1615 cm^{-1} broadband at 1570–1560 cm^{-1} is a region with possible non-matrix contribution, and it was used for nitrate species in soils [108]. However, apart from possible contributions from water and silicates, it may correspond to the strong absorption band of black carbon [56] used as an FTIR–PAS reference, so distortions in possible contributions are unavoidable [52]; this is confirmed by the absence of the band in ATR–FTIR and DRIFT. The H–O–H bands at 1640 cm^{-1} and 1610 cm^{-1}, unbound and more tightly bound water, have different intensity ratios in DRIFT than ATR–FTIR or FTIR–PAS. The band intensity at 1640 cm^{-1} is higher, and this pair is not resolved.

Finally, the secondary peaks appear centered at 1540–1520 cm^{-1}, which may be a manifestation of another overtone band of quartz [105] or Amide II band, although the intensity of this band in all three modalities is relatively low. Carbon–carbon bonds are manifested by 1560 cm^{-1} (alkene/aromatic stretch) and 410 cm^{-1} (in-phase vibrations, [131] see below), but these bands have low intensity and are detectable mainly by FTIR–PAS.

As a whole, the region of 1600–1500 cm^{-1} bears much information but is disadvantageous for quantification with any of the studied modalities unless another reference sample or spectra handling is used.

The second subregion, 450–1170 cm^{-1}, also shows well-defined medium-intensity peaks attributed to overtones and combination bands of O–Si–O bending vibrations in quartz and hydrosilicates, especially 1390, 1280, and 1240 cm^{-1}, each having a SOM counterpart (Table 1). According to existing DRIFT measurements, prominent bands in typical soils are C–H bending vibrations, including aliphatic and aromatic C–H (1300–1500 cm^{-1}) and C–O stretching vibrations from carbonates (1400–1500 cm^{-1}); however, no control over possible inorganic constituents was carried out [107,133].

In this region, the most informative modality is FTIR–PAS. It provides a well-resolved medium-intensity band of symmetric carboxylate band at 1380 cm^{-1} and Amide III bands at 1280 and 1240 cm^{-1}, and the minor (shoulder) band at 1420 cm^{-1} corresponding to C=O stretch. For DRIFT, all these bands have higher intensity, are unresolved, and show a high noise level, so this modality is not preferable in this subregion. On the other hand, ATR–FTIR provides only low-intensity noisy bands and is also almost unusable. The band intensity at 1185 cm^{-1} detected by FTIR–PAS and less reliably with DRIFT depends on the soil type and fraction and thus corresponds to SOM and CH_2 wagging, although these results should not be considered fully reliable due to the low intensity of this band.

In our opinion, the region 1450–1170 cm^{-1} is most challenging to interpret and cannot be used for both SOM and inorganic-component assessment, and requires sophisticated data treatment. Thus, the whole region 1700–1170 cm^{-1} ("SOM region") requires either a sample preparation or at least measurements with several IR modalities.

3.6. Quartz Overtone Region (1170–800 cm^{-1})

The boundary between the previous and this region is made not only from the viewpoint of band attribution to soil components but also modality-wise. In this region, DRIFT and especially FTIR–PAS modalities start to experience saturation effects [88,89], which results in the distorted intensities of matrix bands (Figure 9). As the absorption coefficient of crystalline components of the soil matrix can reach as high as 10000 cm^{-1} at wavenumbers of 1100–500 cm^{-1} [105,134–136], the signal generation shifts from thermally governed conditions of FTIR–PAS to radiation governed mode [52]. Although Table 1 contains some SOM counterparts of these bands, the similarity of the spectra modality-wise rather than sample-wise shows that the silicate matrix dominates this region. The exceptions are bands at 860 and 830 cm^{-1}, corresponding to Al–O vibrations in clay minerals. A low-intensity but very stable peak at 830 cm^{-1} may also be attributed to illite and smectite [123].

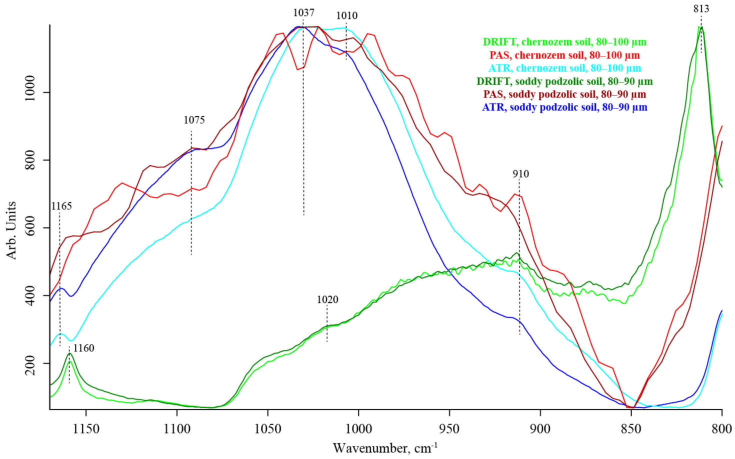

Figure 9. Normalized FTIR spectra in 1170–800 cm^{-1}. DRIFT, ATR, and PAS (IMF 1.6 kHz) spectra of shelterbelt chernozem soil (dry fractionation, 80–100 μm), light green, light blue, and light red, respectively; and DRIFT, ATR, and PAS (IMF 1.6 kHz) spectra of sod-podzolic soil (dry fractionation, 80–90 μm), dark green, dark blue, and dark red, respectively.

The bands of 1160 cm^{-1} and 1080 cm^{-1} correspond to quartz, and the bands at 1037 and 975 cm^{-1} are intense and unresolved. The bands of 1110, 1095, 1080, and 875 cm^{-1}, corresponding to amorphous silica and silicates, are not intense and not well resolved in all three modalities. The band at 1020–950 cm^{-1} is attributed to Si–O from both quartz and clay minerals, with the bands at 950–600 cm^{-1} dominated by the vibrations of (Mg, Al)–OH in clay minerals at 915 cm^{-1} [28]. As a whole, ATR–FTIR becomes the primary source of information in this region as DRIFT and FTIR–PAS start to lose sensitivity and are characterized by a higher noise level.

3.7. Quartz Lattice Region (800–150 cm^{-1})

The mid-IR subregion, 800–400 cm^{-1}, contains the most noticeable quartz lattice vibrations. The bands at 796 and 774 cm^{-1} are intense in all three modalities, though in FTIR–PAS, these peaks are not resolved. The primary quartz band at 697 cm^{-1} is well-resolved and intense in all three modalities and can be considered an internal standard (Figure 10).

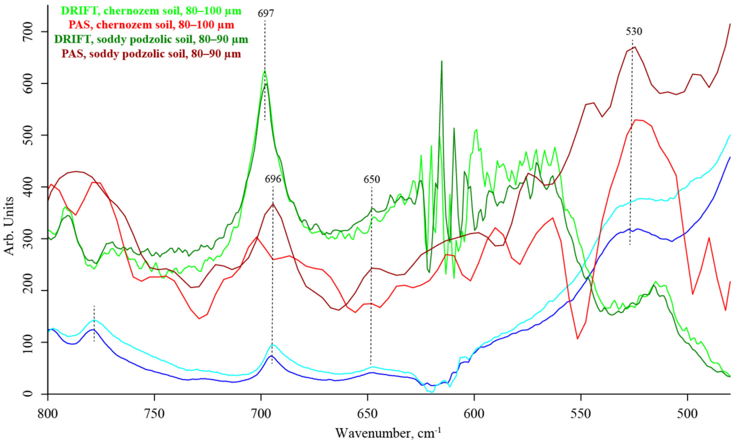

Figure 10. Normalized FTIR spectra in 800–450 cm^{-1}. DRIFT, ATR, and PAS (IMF 1.6 kHz) spectra of shelterbelt chernozem soil (dry fractionation, 80–100 μm), light green, light blue, and light red, respectively; and DRIFT, ATR, and PAS (IMF 1.6 kHz) spectra of sod-podzolic soil (dry fractionation, 80–90 μm), dark green, dark blue, and dark red, respectively.

The band intensities at 715 and 640 cm^{-1} correlate in FTIR–PAS and ATR–FTIR and can be assigned to water librations. DRIFT does not reveal these bands. The weak shoulder band at 670 cm^{-1} does not depend on the modality and somewhat distorts the band at 697 cm^{-1}; it can be assigned to the residual CO_2. The contribution from C–C in-phase vibrations [131] at 430–420 cm^{-1} seems unreliable as this region is dominated by intense clay and quartz vibrations, and the intensity of this band does not seem to depend on the soil type.

The FIR region 400–150 cm^{-1} can be readily united with the short-wavenumber mid-IR region of 800–400 cm^{-1} and provides the information mainly on the quartz part of the inorganic matrix (Figure 11); the only bands that can be attributed to amorphous silica are 395 and 360 cm^{-1}. Bands at 263, 185, and 130 cm^{-1}, and 116–110 cm^{-1} can be attributed to quartz. The band at 330 cm^{-1} could be the manifestation of Mg–O stretch [104] or iron oxide, while the medium-intensity band at 275 cm^{-1} could be attributed to chloride or Ti–O bonds. Bands that most probably are attributed to iron oxides at 700–600, 470, and 330 cm^{-1} are seen in all three modalities (most substantial intensities, ATR–FTIR).

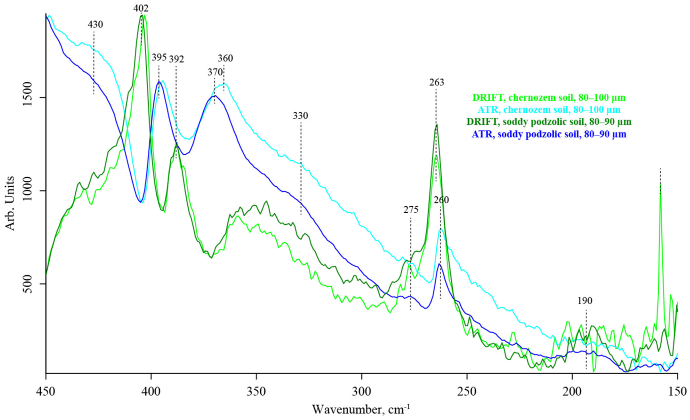

Figure 11. Normalized FTIR spectra in 1170–800 cm^{-1}. DRIFT and ATR spectra of shelterbelt chernozem soil (dry fractionation, 80–100 μm), light green and light blue, respectively; and DRIFT and ATR spectra of sod-podzolic soil (dry fractionation, 80–90 μm), dark green and dark blue, respectively.

In this region, ATR–FTIR provides the largest volume of information on the sample despite the noise level. DRIFT shows only primary bands of SiO_2. Despite a somewhat better resolution of neighboring peaks, FTIR–PAS shows a high noise level and low intensities, making this technique in this region only supporting ATR–FTIR or DRIFT.

4. Discussion

4.1. Common Features of IR Spectra in Different Modalities

Thus, comparing IR spectra of soils of different types and agricultural use allows summing up the modality applicability. The bands that are revealed in all three modalities are hydrogen-bonded SiO–H . . . H_2O stretch (3690–3680 cm^{-1}, ATR–FTIR here is not reliable), methylene stretch bands at 2930–2910 cm^{-1} and 2860–2850 cm^{-1}, and 1390–1380 cm^{-1}, most probably symmetric stretch carboxylate (DRIFT and FTIR–PAS), and 697 cm^{-1}, Si–O–Si bend in SiO_2 [106]. The water bands of 1620–1610 cm^{-1}, 1600–1598 cm^{-1}, and 1580 cm^{-1} HO–H stretch (probably, the latter is carboxylate) appear in the spectra of all three modalities but are unresolved and require data treatment (Table 1).

The bands 2000–1990, 1885, and 1790–1783 cm^{-1}, the SiO_2 overtone triplet, are revealed by DRIFT and FTIR–PAS. Amide I, II, and III bands appear in DRIFT and FTIR–PAS spectra while not in ATR–FTIR. CH vibrations are SOM, except for methylene and carboxylate groups, are not seen in ATR–FTIR. The bands at 1163–1153 cm^{-1}, SiO_2 lattice [106], 1037 cm^{-1}, Si–O asymmetrical stretch Al–O stretch [47], and 796 cm^{-1}, lattice symmetrical Si–O–Si stretch [106,114], are revealed by ATR–FTIR and DRIFT but are not fully resolved in FTIR–PAS. In many cases, each band can have contributions from SOM and inorganic constituents [27,28]; a comparison of DRIFT or FTIR–PAS with ATR–FTIR could provide additional information from the spectral set. High absorption of quartz in the 1110–600 cm^{-1} region, with the saturation effects for DRIFT and FTIR–PAS in the 1110–900 cm^{-1} region, result in much higher intensities of DRIFT/FTIR–PAS overtone bands. Thus, the bands attributed to overtones of SiO_2 bands, 2000–1770, 1600, 1460, 1380, 1280, 1235, and 1185 cm^{-1}, are strong to medium intensity in DRIFT and FTIR–PAS spectra and do not appear in ATR–FTIR.

4.2. DRIFT

The DRIFT modality provides the maximum number of reliably acquired bands (Table 1) and shows the highest overall sensitivity in the whole range, from NIR to FIR. The bands in the NIR region (7500–4500 cm^{-1}) can be used only with this modality due to lower noise, with FTIR–PAS showing only the most intense peaks in DRIFT as weak counterparts. Still, DRIFT may be used with caution due to the particle-size effect [45]. From the viewpoint of quantitative fraction comparison, DRIFT measurements should be corrected to radiation reflections from matrix particles of different sizes [47], and a direct comparison of (sub)millimeter-size and fine (micrometer-size) fractions with DRIFT is not very advantageous.

In addition, using DRIFT for native soil samples may provide saturated bands in the case of high absorption coefficients; thus, this modality requires diluting a sample using a non-absorbing matrix, such as KBr [47]. However, such matrices are not chemically inert and may result in deviations in the spectra compared to unchanged undiluted soil samples. From this point of view, FTIR–PAS of intact samples may be adjusted using the interferometer frequency, which provides less saturation [52]. Therefore, contrary to other studies [35,46,52,81,137] and similarly to our IR modality comparison on nanodiamonds [138], DRIFT modality was implemented using a bare-mirror technique [138]. In this case, a bare mirror serves as the reference sample, decreasing the noise and providing excellent sensitivity and reproducibility, but is more seldom used in practical DRIFT analysis. Thus, this attachment provides diffuse reflection measurements without sample dilution, and thus, much more valuable information from diffuse reflectance spectra. This technique allows diffuse reflectance measurements without sample dilution with KBr, thus without changing the reproducibility and sensitivity [138].

Apart from the whole studied NIR region, DRIFT is most valuable for the CH region (3000–2800 cm^{-1}) and one of the most difficult from the viewpoint of the information, 1700–1200 cm^{-1}. This modality is also capable of hydrogen-bond continua at 3900–3000 cm^{-1}, only with FTIR–PAS somewhat superior, though with a higher-level noise. DRIFT provides the maximum sensitivity towards hydrocarbon constituents: CH_X groups at 3000–2700 cm^{-1}, though FTIR–PAS is capable of measuring alkene and aromatic bands, which are hidden in DRIFT by the low-wavenumber shoulder of the OH continuum. Similar to the previous study on nanodiamonds [138], DRIFT shows relatively intense bands at 1460–1310 cm^{-1} between Amide II and Amide III groups corresponding to CH_2/CH_3 deformation, although these bands could also have oxygen-containing components [112,113]. The region of 1170–400 cm^{-1} has the secondary value due to DRIFT saturation and lower sensitivity. However, most primary quartz and hydrosilicate bands are distinguishable for all the soil samples. Compared to nanodiamond modality comparison [138], the region 2300–2000 cm^{-1} is not very informative in DRIFT and FTIR–PAS despite a relatively high noise level.

Thus, within the frames of the bare-mirror technique used in this study, DRIFT can soil survey analysis in the broader region and with sufficient sensitivity; thus, it could be considered the primary modality for this task. FTIR–PAS could be considered as an alternative, ATR–FTIR as a complementing modality.

4.3. ATR–FTIR

Due to low sensitivity in the NIR and mid-IR region of 7500–2000 cm^{-1}, the ATR–FTIR spectrum shows little to no information in this region, with the only exception of methylene CH_2 bands for chernozem soils. In the region of 2800–2000 cm^{-1}, most bands in ATR–FTIR mode are artifact bands that should be excluded from the consideration.

In the region of 200–1200 cm^{-1}, the possibilities of the ATR–FTIR modality become almost the same as DRIFT and FTIR–PAS in water bands and inorganic matrix, but the sensitivity towards band attributed to SOM in this region is much lower than other two modalities.

Other primary bands in ATR–FTIR spectra are H–O–H bending vibrations (loosely bound, 1643 cm^{-1}, and tightly bound, 1620–1600 cm^{-1}), and compared to DRIFT or FTIR–PAS, the intensity of the band at 1640 cm^{-1} is higher than the other band, and they are not well-resolved in all the soil samples.

It is noteworthy that ATR–FTIR is more sensitive to the matrix than functional groups on the surface due to their lower contribution; a similar picture was found for other functional materials probed by two modalities [138].

ATR–FTIR becomes the most helpful modality for the region of 1170 cm^{-1} and below when DRIFT and FTIR–PAS show weaker, shoulder, or enveloping bands, and FTIR–PAS also shows significant saturation effects [52] and high noise levels. However, the most intense bands still correspond to the inorganic matrix, and this modality shows the maximum number of bands. Especially evident is the region 600–100 cm^{-1}, when FTIR–PAS spectra show low-intensity and high noise, while DRIFT shows only primary SiO_2 bands. Thus, in our opinion, an essential feature of ATR–FTIR in the low-wavenumber region is high intensities of bands that cannot be attributed to SiO_2 and should correspond to clay minerals or other oxides such as hematite, magnetite and rutile, and anions [129].

Thus, in concordance with the previous findings for chernozem soils [27,52], ATR–FTIR provides the best resolution for primary structural modes of the SiO_2 lattice vibrations in the 1150–100 cm^{-1} region, showing no absorption saturation at the ATR–FTIR penetration depth, while DRIFT and especially FTIR–PAS measurements (in the region 1110–800 cm^{-1}) experience a severe change in relative peak heights due to the saturation effects [52]. However, ATR–FTIR provides mediocre sensitivity towards the medium and minor bands attributed to carbon-oxygen bonds.

The detector sensitivity is crucial in ATR–FTIR, and a room-temperature DLaTGs detector can be recommended for primary band monitoring [138]. In contrast, a photovoltaic detector severely increases the spectral information, making ATR–FTIR closer to FTIR–PAS while retaining all ATR–FTIR advantages previously shown for nanodiamonds [138].

Thus, ATR–FTIR is preferable in the 2000–1200 cm^{-1} region due to its higher sensitivity, lower effects from gaseous water, and better resolution in this region when DRIFT and FTIR–PAS experience optical or thermal saturation. ATR–FTIR is most informative for the inorganic matrix, and both DRIFT and FTIR–PAS can be considered complementary. However, for SOM-based band intensities and minor oxygen-containing groups, the sample comparison by ATR–FTIR is less expedient; DRIFT or FTIR–PAS should be used instead.

4.4. FTIR–PAS

Contrary to DRIFT, especially in rapid-scan modes (IMF of 1.6 and 2.5 kHz), FTIR–PAS spectra are affected with thermal penetration depth governed by thermophysical parameters of the matrix and almost independent from the particle size [138]. Thus, FTIR–PAS spectra are directly comparable from the composition retaining most DRIFT features unrevealed in ATR–FTIR spectra. In modalities used in this study, no significant differences between FTIR–PAS and DRIFT spectra were observed in the whole mid-IR region of 4000–400 cm^{-1}. FTIR–PAS spectra are similar to DRIFT and show approximately the same intensity ratios for similar bands (CH_x, water, overtone SiO_2). As discussed above, the used DRIFT is not practical in the NIR region due to the high noise level, which reveals only primary water bands. However, in the whole region 4000–1700 cm^{-1}, FTIR–PAS can be considered the primary technique for soil analysis rivaling or complementing DRIFT.

In the region of 4000–3600 cm^{-1}, FTIR–PAS exhibits weak stretching vibration bands of isolated hydrogen-bonded species at 3740 cm^{-1} [139], which is not visible with other modalities, as well as bands at 3670, 3630, and 3540 cm^{-1}, and the sensitivity towards primary bands of hydrogen-bonded species, 3695 and 3620 cm^{-1}, is the same as in DRIFT.

Bands of methylene and methyl vibrations in the region 2980–2800 cm^{-1} are pronounced, and the sensitivity is the same as DRIFT, but the higher sensitivity of FTIR–PAS provides a series of weak but distinguishable bands that can be attributed to alkene and aromatic compounds that cannot be revealed in DRIFT without data treatment.

The region 2700–2000 cm^{-1} is very interesting as FTIR–PAS is the only modality in this region that provides reliable information; here, most valuable is the pronounced doublet at 2360 and 2340 cm^{-1} that can be attributed to absorbed CO_2 peaks and higher overtone bands of SiO_2 at 2250 and 2160 cm^{-1}. DRIFT in this region provides similar information but with much less pronounced bands.

The bands at 1640 and 1600 cm^{-1} are intense and have the same ratio as in DRIFT, though FTIR–PAS provides slightly better resolution (these are maximum-resolved). As was found previously [138], FTIR–PAS in 1700–1500 cm^{-1} shows a significant effect from water vapor bands leading to an intense noise of sharp negative bands. Thus, DRIFT seems more expedient in this region from the viewpoint of sensitivity and reliability.

In addition, FTIR–PAS provides high intensities of bands at 1540, 1460, and 1400 cm^{-1}, almost entirely unresolved in DRIFT and very weak in ATR–FTIR. However, all these are spurious as they may correspond to SiO_2 combination/overtones and functional groups of SOM. A two-modality concept, i.e., simultaneous use of two complementary modalities with different but reliable spectra, might provide more information, but DRIFT spectra cannot be used without data treatment, so this problem requires a more complex solution. The region 1400–1200 cm^{-1} in FTIR–PAS is less resolved than ATR–FTIR but still has a higher sensitivity.

For the region below 1200 cm^{-1}, the value of the FTIR–PAS modality rapidly decreases due to saturation effects [88,89] of highly absorbing SiO_2 bands [52], the overall decrease in the band intensity due to a decrease in the IR source intensity, and an increase in the noise. Therefore, it is almost unusable in 1100–800 cm^{-1}, at least with complex data treatment, which is not expedient compared to DRIFT and ATR–FTIR.

Comparison of FTIR–PAS with ATR–FTIR shows almost the same situation as DRIFT with ATR–FTIR: SiO_2 matrix vibration intensities in FTIR–PAS are degraded, although primary bands are distinct. Thus, FTIR–PAS can be considered a primary modality in the CH and SOM regions, where its possibilities are equal or somewhat superior to DRIFT, and it is almost entirely complementary to ATR–FTIR. Still, in the whole region, the DRIFT modality provides better possibilities for band assessment.

4.5. Summary. Modality Comparison

Thus, DRIFT seems to be the most appropriate choice of all the three modalities for soil survey and qualitative assessment (Figure 12). First, it provides good sensitivity, especially with a photovoltaic detector, in the region when SOM bands are manifested. The best sensitivity of DRIFT is in hydrogen-bond, CH_x, and C=O/water bands. Second, DRIFT is characterized by the broadest spectral region (7500–200 cm^{-1}) with essential information; DRIFT is the only reliable technique in the NIR region (7500–4000 cm^{-1}) due to lower noise as a single-channel technique and FIR region.

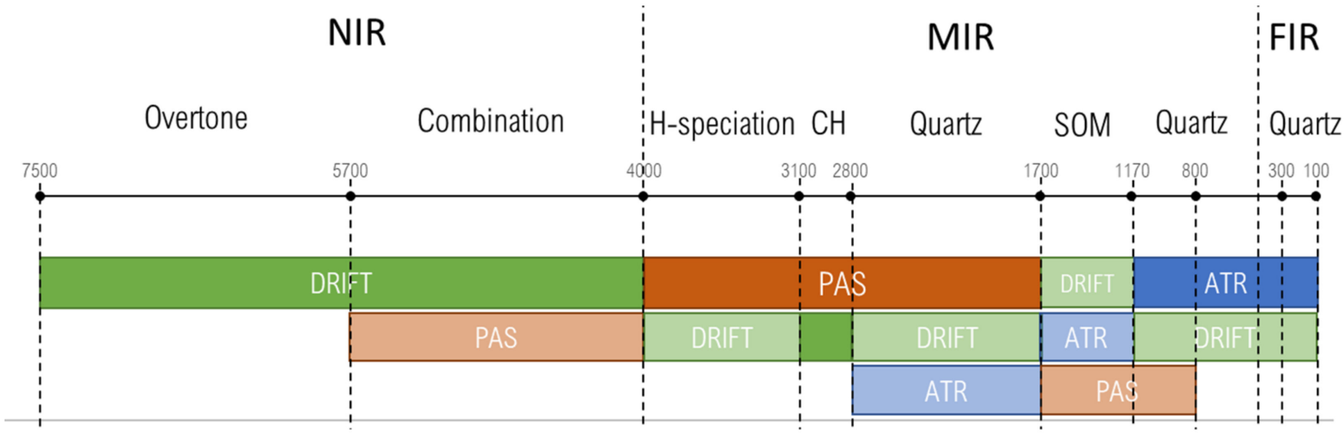

Figure 12. Applicability of DRIFT, ATR–FTIR, and FTIR–PAS for qualitative soil analysis for silicate soils. Applicable techniques are shown in full colors, ambiguous, in watercolors, most informative technique in each subregion (see the text for details) is shown at a higher position.

Comparison of DRIFT with ATR–FTIR shows that while ATR–FTIR provides additional information in the FIR region, DRIFT can survey this region (Figure 12). From the viewpoint of SOM assessment, FTIR–PAS is similar to DRIFT [47]. With the same sensitivity as DRIFT with a room-temperature DLaTGs detector and lower sensitivity than DRIFT with a photovoltaic detector.

ATR–FTIR and DRIFT/FTIR–PAS modalities are somewhat complementary. ATR–FTIR in the 2000–1200 cm^{-1} region is expedient as a second technique with DRIFT or FTIR–PAS (Figure 12). In addition, ATR–FTIR has the advantage of a small sample amount. However, the lower radiation intensity and low optical penetration depths in ATR–FTIR do not allow revealing the overtone and combination bands of matrix minerals (Table 1). They can be revealed only for a long accumulation time with low signal-to-noise ratios [52]. Thus, contrary to DRIFT and FTIR–PAS, ATR–FTIR cannot use a reliable internal standard in the region of 4000–2000 cm^{-1}, which, along with low sensitivity, makes this modality less expedient in this region.

Along with higher noise, FTIR–PAS, especially at a single IMF, cannot be recommended as a primary IR technique (Figure 12). However, its main feature is lower dependence on particle size due to significant signal penetration depth. Thus, it can be a support or check technique for either DRIFT or ATR–FTIR. Furthermore, from the viewpoint of inorganic soil constituents, FTIR–PAS provides more detailed information under the same conditions than DRIFT, though ATR–FTIR excels FTIR–PAS, consistent with the existing data [31,79]. Another feature of FTIR–PAS is depth profiling by an IMF change, which affects the spectra [52] and can be used to investigate the thermal properties of soils. In addition, the disadvantage of this modality is a high penetration depth (up to 1 mm), which requires rather large sample volumes to eliminate the effect of sample support on the spectra, which could be a problem for fine and ultrafine fractions.

Though it is rather apparent that all the modalities can provide the relevant information on soil composition, contrary to comparison for complex objects [35,46,52,81,137] and some previous studies on soils [47,52,55], we cannot conclude that all the IR modalities can be used alone in soil characterization, as no single modality provides the complete information. Thus, a combination of two or three modalities seems essential.

Thus, we can describe four tasks for IR of silicate soil samples.

1. A survey of SOM in specific samples (soil types, layers, or similar tasks)—the primary bands of CH_x, Amide I–III region, and carboxylate groups—may be implemented with DRIFT and FTIR–PAS. DRIFT can be used in the broadest region for all soil types and fractions; ATR–FTIR could be selected from the viewpoint of simplicity and rapidity and does not require a sensitive detector, though some SOM bands may not be revealed; FTIR–PAS at a low IMF with a check of artifacts from gaseous water can be used the same way as DRIFT.
2. A survey of inorganic matrix soil constituents in particular samples (specific soil types, layers, aggregates, fractions), DRIFT should be selected as the primary modality to have the highest sensitivity; ATR–FTIR can also be used as a primary technique but would still require a sensitive detector for the region 2000–1000 cm^{-1}.
3. A more widespread and general task of soil comparison simultaneously by SOM and inorganic bands should rely on at least two IR modalities. In this case, DRIFT should be the primary modality to have the highest sensitivity for assessing the maximum number of all the bands. ATR–FTIR and FTIR–PAS cannot be recommended as primary modalities due to low sensitivity in some parts of the spectra and high noise levels. However, DRIFT/ATR–FTIR or FTIR–PAS/ATR–FTIR should be used; most likely, all three modalities may provide the complete picture.
4. Finally, a task for FTIR may compare differences in similar samples. For this task, all three modalities should be used together. In this case, DRIFT with a high-sensitive detector is a primary technique used to survey the whole spectrum in the NIR region and mid-IR region 4000–1200 cm^{-1}. It is used to cross-check the major hydrogen-bond, C–H, and HOH bands. ATR–FTIR at 2000–300 cm^{-1} is used to continue the most information-bearing spectrum from 1500 cm^{-1} to 150 cm^{-1}. DRIFT and ATR–FTIR can be normalized using three major SiO_2 bands at 697 cm^{-1}, 395 cm^{-1}, and 265 cm^{-1}. The region 4000–1500 cm^{-1} should be covered by DRIFT and FTIR–PAS, and the spectra should be normalized with the triplet at 2000–1700 cm^{-1}. The region 1500–900 cm^{-1} should be assessed with all three modalities (preferably, FTIR–PAS at two IMFs, a rapid and a slow scan mode). This approach would reveal possible artifact bands, optical/thermal saturation and provide information on the nature of complex bands. As we mentioned above, DRIFT measurements should be corrected to radiation reflections from matrix particles, and FTIR–PAS or ATR–FTIR may be a valuable addition as less dependent on the particle size.

The quantification was not considered in this study in detail as a separate and complex problem. However, the interrelationships between the spectra of all three modalities can be summed up as follows. First of all, if a single or several modalities are used, an internal standard should be selected. For rather obvious reasons, it should be selected among the SiO_2 bands. The most convenient bands for DRIFT or FTIR–PAS are overtones of quartz lattice vibrations at 2000–1700 cm^{-1}. For similar samples, which are not different in the hydrogen bonds, the band at 3690 cm^{-1} could also be used. Though it contains some vital information, the region of 1100–400 cm^{-1} seems most troublesome from the quantification viewpoint due to possible optical and thermal-saturation effects in DRIFT and FTIR–PAS and relatively high noise levels in spectra. In this region, possible contributions of different constituents are almost impossible to distinguish using data treatment and sample treatment. Here, FTIR spectroscopy alone cannot give the whole answer, and other techniques are very expedient [27,32]. Apart from internal standards, this requires a reference method for SOM (NMR or optical spectroscopy, or their use along with FTIR using 2D-COS techniques [140–144]), for the exact values of absorption coefficients for these bands that can seriously facilitate quantitative analysis. Furthermore, the quantification data should be handled with chemometric models [59,145], and integrated peak intensities should probably be used [52].

5. Conclusions

From the viewpoint of qualitative analysis of silicate soils by FTIR spectrometry in a wide wavelength range, rapid and non-destructive analysis and comparison of soils for the majority of tasks solved by IR spectroscopy should be based upon all three modalities, diffuse reflectance, attenuated total reflection, and photoacoustic. DRIFT provides the maximum number of bands among all three modalities in the whole region and is capable of measuring most SOM bands. ATR–FTIR provides the maximum sensitivity for the matrix absorption region (1100–150 cm^{-1}). FTIR–PAS reveals more bands than DRIFT and ATR–FTIR in the region 4000–1500 cm^{-1} and provides information less dependent on the particle size. Overall, both DRIFT and FTIR–PAS can be considered primary techniques for SOM quantification due to a low noise level and sensitivity, while ATR–FTIR, for inorganic matrix. In addition, DRIFT shows the maximum possibility of hydrocarbon contents, especially with a photovoltaic detector.

The methodological approaches for the combined use of several IR techniques and previous findings on interpreting individual spectra and sample preparation seem reliable for using in soil analysis, including meso- and microaggregate levels. Moreover, this approach, either in separate regions or a wide wavelength range, can be used for similar complex samples such as humic substances, biochars, or organomineral complexes due to overlapping spectra from organic, water, and mineral components.

Supplementary Materials: The following are available online at https://www.mdpi.com/article/10.3390/agronomy11091879/s1, Figure S1: Location of sampling points, a map and satellite pictures. Experimental field of the Zelenograd station of the V.V. Dokuchaev Soil Institute (village of Eldigino, Moscow region, Russia) Red markers on both images are agrosodpodzolic soil. the coordinates of the sampling site are 56° 07′ 56″ N 37° 48′ 09″ E, Figure S2: Location of sampling points. A, the positions of natural steppe (red marker, V.V. Alekhin Tsentralno-Chernozemny Nature Reserve) and agrogenic soils (yellow-star marker, Kursk Research Institute of Agricultural Production), Figure S3: Location of sampling points. Points of selection of agrogenically transformed soils: markers: B, shelterbelt since 1964, E- arable cropland under wheat, Figure S4: Normalized FTIR spectra in the range 4000–150 cm–1. DRIFT, ATR, and PAS (IMF, 1.6 kHz) spectra of shelterbelt chernozem soil (dry fractionation, 80–100 µm), light green, light blue, and light red, respectively; and DRIFT, ATR, and PAS (IMF, 1.6 kHz) spectra of soddy podzolic soil (dry fractionation, 80–90 µm), dark green, dark blue, and dark red, respectively, Table S1: Parameters of recording spectra by DRIFT, Table S2: Parameters of recording spectra by ATR–FTIR, Table S3: Parameters of recording spectra by FTIR–PAS.

Author Contributions: Conceptualization, M.A.P.; methodology, D.S.V. and O.B.R.; formal analysis, M.A.P., O.B.R. and D.S.V.; investigation, D.S.V. and O.B.R.; resources, D.S.V.; data curation, D.S.V.; writing—original draft preparation, M.A.P.; writing—review and editing, M.A.P., D.S.V. and O.B.R.; visualization, D.S.V.; supervision, M.A.P.; project administration, M.A.P.; funding acquisition, M.A.P. All authors have read and agreed to the published version of the manuscript.

Funding: This work was supported by The Russian Science Foundation, project number 19-13-00117.

Data Availability Statement: Not applicable.

Acknowledgments: This research was performed according to the Development program of the Interdisciplinary Scientific and Educational School of Lomonosov Moscow State University, “The future of the planet and global environmental change”.

Conflicts of Interest: The authors declare no conflict of interest.

References

1. Ichwana, I.; Nasution, Z.; Munawar, A.A. The application of fourier transform infrared photoacoustics spectroscopy (FTIR-PAS) for rapid soil quality evaluation. *Rona Tek. Pertan.* **2017**, *1*, 1–10. [CrossRef]
2. Volkov, D.S.; Rogova, O.B.; Proskurnin, M.A. Photoacoustic and photothermal methods in spectroscopy and characterization of soils and soil organic matter. *Photoacoustics* **2020**, *17*, 100151. [CrossRef] [PubMed]
3. Imeson, A. *Desertification, Land Degradation and Sustainability*; Wiley: Chichester, UK, 2012.
4. Boix-Fayos, C.; Calvo-Cases, A.; Imeson, A.C.; Soriano-Soto, M.D. Influence of soil properties on the aggregation of some Mediterranean soils and the use of aggregate size and stability as land degradation indicators. *Catena* **2001**, *44*, 47–67. [CrossRef]
5. Delelegn, Y.T.; Purahong, W.; Blazevic, A.; Yitaferu, B.; Wubet, T.; Goransson, H.; Godbold, D.L. Changes in land use alter soil quality and aggregate stability in the highlands of northern Ethiopia. *Sci. Rep.* **2017**, *7*, 1–12. [CrossRef]
6. Sorour, M.M.; Saleh, M.M.; Mahmoud, R.A. Thermal conductivity and diffusivity of soil. *Int. Commun. Heat Mass Transf.* **1990**, *17*, 189–199. [CrossRef]
7. Bristow, K.L.; Kluitenberg, G.J.; Goding, C.J.; Fitzgerald, T.S. A small multi-needle probe for measuring soil thermal properties, water content and electrical conductivity. *Comput. Electron. Agric.* **2001**, *31*, 265–280. [CrossRef]
8. Jong van Lier, Q.d.; Durigon, A. Soil thermal diffusivity estimated from data of soil temperature and single soil component properties. *Rev. Bras. Ciência Solo* **2013**, *37*, 106–112. [CrossRef]
9. Józefaciuk, G.; Sławiński, C.; Walczak, R.T.; Bieganowski, A. *Review of Current Problems in Agrophysics*; Inst. of Agrophysics PAS: Lublin, Poland, 2005.
10. Lal, R. Soil carbon sequestration impacts on global climate change and food security. *Science* **2004**, *304*, 1623–1627. [CrossRef]
11. Chen, Y.; Zou, C.; Mastalerz, M.; Hu, S.; Gasaway, C.; Tao, X. Applications of micro-fourier transform infrared spectroscopy (FTIR) in the geological sciences–A review. *Int. J. Mol. Sci.* **2015**, *16*, 30223–30250. [CrossRef]
12. Falkowski, P.; Scholes, R.J.; Boyle, E.; Canadell, J.; Canfield, D.; Elser, J.; Gruber, N.; Hibbard, K.; Hogberg, P.; Linder, S.; et al. The global carbon cycle: A test of our knowledge of earth as a system. *Science* **2000**, *290*, 291–296. [CrossRef]
13. Pansu, M.; Gautheyrou, J. Characterization of humic compounds. In *Handbook of Soil Analysis: Mineralogical, Organic and Inorganic Methods*; Springer: Berlin/Heidelberg, Germany, 2006; pp. 399–451.
14. Christensen, B.T. Physical fractionation of soil and organic matter in primary particle size and density separates. In *Advances in Soil Science*; Stewart, B.A., Ed.; Advances in Soil Science; Springer: New York, NY, USA, 1992; pp. 1–90.
15. Fultz, L.M.; Moore-Kucera, J.; Calderón, F.; Acosta-Martínez, V. Using fourier-transform mid-infrared spectroscopy to distinguish soil organic matter composition dynamics in aggregate fractions of two agroecosystems. *Soil Sci. Soc. Am. J.* **2014**, *78*, 1940–1948. [CrossRef]
16. Ge, Y.; Thomasson, J.A.; Morgan, C.L.S. Mid-infrared attenuated total reflectance spectroscopy for soil carbon and particle size determination. *Geoderma* **2014**, *213*, 57–63. [CrossRef]
17. Tinti, A.; Tugnoli, V.; Bonora, S.; Francioso, O. Recent applications of vibrational mid-Infrared (IR) spectroscopy for studying soil components: A review. *J. Cent. Eur. Agric.* **2015**, *16*, 1–22. [CrossRef]
18. Linker, R. Application of FTIR spectroscopy to agricultural soils analysis. In *Fourier Transforms—New Analytical Approaches and FTIR Strategies*; Nikolic, G., Ed.; InTech: London, UK, 2011; pp. 385–404.
19. Rossel, R.V.; Walvoort, D.J.J.; McBratney, A.B.; Janik, L.J.; Skjemstad, J.O. Visible, near infrared, mid infrared or combined diffuse reflectance spectroscopy for simultaneous assessment of various soil properties. *Geoderma* **2006**, *131*, 59–75. [CrossRef]
20. Volkov, D.S.; Rogova, O.B.; Proskurnin, M.A. Temperature dependences of IR spectra of humic substances of brown coal. *Agronomy* **2021**, *11*, 1822. [CrossRef]
21. Yuan, Y.; Cai, X.; Tan, B.; Zhou, S.; Xing, B. Molecular insights into reversible redox sites in solid-phase humic substances as examined by electrochemical in situ FTIR and two-dimensional correlation spectroscopy. *Chem. Geol.* **2018**, *494*, 136–143. [CrossRef]
22. Karpukhina, E.; Mikheev, I.; Perminova, I.; Volkov, D.; Proskurnin, M. Rapid quantification of humic components in concentrated humate fertilizer solutions by FTIR spectroscopy. *J. Soils Sed.* **2018**, *19*, 2729–2739. [CrossRef]
23. Boguta, P.; Sokołowska, Z.; Skic, K. Use of thermal analysis coupled with differential scanning calorimetry, quadrupole mass spectrometry and infrared spectroscopy (TG-DSC-QMS-FTIR) to monitor chemical properties and thermal stability of fulvic and humic acids. *PLoS ONE* **2017**, *12*, e0189653. [CrossRef] [PubMed]
24. Morra, M.J.; Marshall, D.B.; Lee, C.M. FT-IR analysis of aldrich humic acid in water using cylindrical internal reflectance. *Commun. Soil Sci. Plant. Anal.* **2008**, *20*, 851–867. [CrossRef]
25. Tatzber, M.; Stemmer, M.; Spiegel, H.; Katzlberger, C.; Haberhauer, G.; Mentler, A.; Gerzabek, M.H. FTIR-spectroscopic characterization of humic acids and humin fractions obtained by advanced NaOH, Na4P2O7, and Na2CO3 extraction procedures. *J. Plant. Nutr. Soil Sci.* **2007**, *170*, 522–529. [CrossRef]
26. Tanykova, N.; Petrova, Y.; Kostina, J.; Kozlova, E.; Leushina, E.; Spasennykh, M. Study of organic matter of unconventional reservoirs by IR Spectroscopy and IR microscopy. *Geosciences* **2021**, *11*, 277. [CrossRef]
27. Dudek, M.; Kabała, C.; Łabaz, B.; Mituła, P.; Bednik, M.; Medyńska-Juraszek, A. Mid-infrared spectroscopy supports identification of the origin of organic matter in soils. *Land* **2021**, *10*, 215. [CrossRef]
28. Slaný, M.; Jankovič, L'.; Madejová, J. Structural characterization of organo-montmorillonites prepared from a series of primary alkylamines salts: Mid-IR and near-IR study. *Appl. Clay Sci.* **2019**, *176*, 11–20. [CrossRef]

29. Madejová, J.; Sekeráková, L'.; Bizovská, V.; Slaný, M.; Jankovič, L'. Near-infrared spectroscopy as an effective tool for monitoring the conformation of alkylammonium surfactants in montmorillonite interlayers. *Vib. Spectrosc.* **2016**, *84*, 44–52. [CrossRef]
30. Du, C.; Wang, J.; Zhou, Z.; Shen, Y.; Zhou, J. In situ measurement of ammonia concentration in soil headspace using fourier transform mid-infrared photoacoustic spectroscopy. *Pedosphere* **2015**, *25*, 605–612. [CrossRef]
31. Du, C.; Zhou, J. Evaluation of soil fertility using infrared spectroscopy: A review. *Environ. Chem. Lett.* **2008**, *7*, 97–113. [CrossRef]
32. Ma, F.; Du, C.; Zhang, Y.; Xu, X.; Zhou, J. LIBS and FTIR–ATR spectroscopy studies of mineral–organic associations in saline soil. *Land Degrad. Dev.* **2020**, *32*, 1786–1795. [CrossRef]
33. Woolverton, P.; Dragila, M.I. Characterization of hydrophobic soils: A novel approach using mid-infrared photoacoustic spectroscopy. *Appl. Spectrosc.* **2014**, *68*, 1407–1410. [CrossRef]
34. Xie, H.T.; Yang, X.M.; Drury, C.F.; Yang, J.Y.; Zhang, X.D. Predicting soil organic carbon and total nitrogen using mid- and near-infrared spectra for Brookston clay loam soil in Southwestern Ontario, Canada. *Can. J. Soil Sci.* **2011**, *91*, 53–63. [CrossRef]
35. Calderón, F.J.; Mikha, M.M.; Vigil, M.F.; Nielsen, D.C.; Benjamin, J.G.; Reeves, J.B. Diffuse-reflectance mid-infrared spectral properties of soils under alternative crop rotations in a semi-arid climate. *Commun. Soil Sci. Plant. Anal.* **2011**, *42*, 2143–2159. [CrossRef]
36. Stenberg, B.; Rossel, R.A.V.; Mouazen, A.M.; Wetterlind, J. Visible and near infrared spectroscopy in soil science. *Adv. Agron.* **2010**, *107*, 163–215.
37. Du, C.; Zhou, J.; Wang, H.; Chen, X.; Zhu, A.; Zhang, J. Determination of soil properties using Fourier transform mid-infrared photoacoustic spectroscopy. *Vib. Spectrosc.* **2009**, *49*, 32–37. [CrossRef]
38. Spence, A.; Kelleher, B.P. FT-IR spectroscopic analysis of kaolinite–microbial interactions. *Vib. Spectrosc.* **2012**, *61*, 151–155. [CrossRef]
39. Niemeyer, J.; Chen, Y.; Bollag, J.M. Characterization of humic acids, composts, and peat by diffuse reflectance fourier-transform infrared spectroscopy. *Soil Sci. Soc. Am. J.* **1992**, *56*, 135–140. [CrossRef]
40. Tatzber, M.; Stemmer, M.; Spiegel, H.; Katzlberger, C.; Haberhauer, G.; Gerzabek, M.H. An alternative method to measure carbonate in soils by FT-IR spectroscopy. *Environ. Chem. Lett.* **2006**, *5*, 9–12. [CrossRef]
41. Wang, S.; Zhang, Z.; Yin, X.; Wang, N.; Chen, D. Influences of nitrogen application levels on properties of humic acids in chernozem amended with different types of organic materials. *Sustainability* **2019**, *11*, 5405. [CrossRef]
42. Minasny, B.; Tranter, G.; McBratney, A.B.; Brough, D.M.; Murphy, B.W. Regional transferability of mid-infrared diffuse reflectance spectroscopic prediction for soil chemical properties. *Geoderma* **2009**, *153*, 155–162. [CrossRef]
43. Reeves, J.B. Near- versus mid-infrared diffuse reflectance spectroscopy for soil analysis emphasizing carbon and laboratory versus on-site analysis: Where are we and what needs to be done? *Geoderma* **2010**, *158*, 3–14. [CrossRef]
44. Yeasmin, S.; Singh, B.; Johnston, C.T.; Sparks, D.L. Evaluation of pre-treatment procedures for improved interpretation of mid infrared spectra of soil organic matter. *Geoderma* **2017**, *304*, 83–92. [CrossRef]
45. Leue, M.; Ellerbrock, R.H.; Bänninger, D.; Gerke, H.H. Impact of soil microstructure geometry on DRIFT spectra: Comparisons with beam trace modeling. *Soil Sci. Soc. Am. J.* **2010**, *74*, 1976–1986. [CrossRef]
46. Brown, D.J.; Shepherd, K.D.; Walsh, M.G.; Mays, M.D.; Reinsch, T.G. Global soil characterization with VNIR diffuse reflectance spectroscopy. *Geoderma* **2006**, *132*, 273–290. [CrossRef]
47. Nguyen, T.T.; Janik, L.J.; Raupach, M. Diffuse reflectance infrared fourier transform (DRIFT) spectroscopy in soil studies. *Soil Res.* **1991**, *29*, 49–67. [CrossRef]
48. Mandelis, A.; Boroumand, F.; Van den Bergh, H. Quantitative diffuse reflectance and transmittance spectroscopy of loosely packed powders. *Spectrochim. Acta A Mol. Spectrosc.* **1991**, *47*, 943–971. [CrossRef]
49. Artz, R.R.; Chapman, S.J.; Robertson, A.J.; Potts, J.; Laggoun-Défarge, F.; Gogo, S.; Comont, L.; Disnar, J.-R.; Francez, A.-J. FTIR spectroscopy can be used as a screening tool for organic matter quality in regenerating cutover peatlands. *Soil Biol. Biochem.* **2008**, *40*, 515–527. [CrossRef]
50. Artz, R.; Chapman, S.; Campbell, C.D. Substrate utilisation profiles of microbial communities in peat are depth dependent and correlate with whole soil FTIR profiles. *Soil Biol. Biochem.* **2006**, *38*, 2958–2962. [CrossRef]
51. Fernandes, A.N.; Giovanela, M.; Esteves, V.I.; Sierra, M.M.d.S. Elemental and spectral properties of peat and soil samples and their respective humic substances. *J. Mol. Struct.* **2010**, *971*, 33–38. [CrossRef]
52. Krivoshein, P.K.; Volkov, D.S.; Rogova, O.B.; Proskurnin, M.A. FTIR photoacoustic spectroscopy for identification and assessment of soil components: Chernozems and their size fractions. *Photoacoustics* **2020**, *18*, 100162. [CrossRef] [PubMed]
53. Xing, Z.; Tian, K.; Du, C.; Li, C.; Zhou, J.; Chen, Z. Agricultural soil characterization by FTIR spectroscopy at micrometer scales: Depth profiling by photoacoustic spectroscopy. *Geoderma* **2019**, *335*, 94–103. [CrossRef]
54. Vaudour, E.; Cerovic, Z.G.; Ebengo, D.M.; Latouche, G. Predicting key agronomic soil properties with UV-Vis fluorescence measurements combined with Vis-NIR-SWIR reflectance spectroscopy: A farm-scale study in a Mediterranean viticultural agroecosystem. *Sensors* **2018**, *18*, 1157. [CrossRef] [PubMed]
55. Yeasmin, S.; Singh, B.; Johnston, C.T.; Sparks, D.L. Organic carbon characteristics in density fractions of soils with contrasting mineralogies. *Geochim. Cosmochim. Acta* **2017**, *218*, 215–236. [CrossRef]
56. Janik, L.J.; Merry, R.H.; Forrester, S.T.; Lanyon, D.M.; Rawson, A. rapid prediction of soil water retention using mid infrared spectroscopy. *Soil Sci. Soc. Am. J.* **2007**, *71*, 507–514. [CrossRef]

57. Jahn, B.R.; Linker, R.; Upadhyaya, S.K.; Shaviv, A.; Slaughter, D.C.; Shmulevich, I. Mid-infrared spectroscopic determination of soil nitrate content. *Biosys. Eng.* **2006**, *94*, 505–515. [CrossRef]
58. Linker, R.; Weiner, M.; Shmulevich, I.; Shaviv, A. Nitrate determination in soil pastes using attenuated total reflectance mid-infrared spectroscopy: Improved accuracy via soil identification. *Biosys. Eng.* **2006**, *94*, 111–118. [CrossRef]
59. Linker, R.; Shmulevich, I.; Kenny, A.; Shaviv, A. Soil identification and chemometrics for direct determination of nitrate in soils using FTIR-ATR mid-infrared spectroscopy. *Chemosphere* **2005**, *61*, 652–658. [CrossRef] [PubMed]
60. Liu, L.; Huan, H.; Zhang, M.; Shao, X.; Zhao, B.; Cui, X.; Zhu, L. Photoacoustic spectrometric evaluation of soil heavy metal contaminants. *IEEE Photonics J.* **2019**, *11*, 1–7. [CrossRef]
61. Xing, Z.; Du, C.; Tian, K.; Ma, F.; Shen, Y.; Zhou, J. Application of FTIR-PAS and Raman spectroscopies for the determination of organic matter in farmland soils. *Talanta* **2016**, *158*, 262–269. [CrossRef]
62. Du, C.; Linker, R.; Shaviv, A. Identification of agricultural Mediterranean soils using mid-infrared photoacoustic spectroscopy. *Geoderma* **2008**, *143*, 85–90. [CrossRef]
63. Du, C.; Linker, R.; Shaviv, A. Characterization of soils using photoacoustic mid-infrared spectroscopy. *Appl. Spectrosc.* **2007**, *61*, 1063–1067.
64. Manhães, R.S.T.; Auler, L.T.; Sthel, M.S.; Alexandre, J.; Massunaga, M.S.O.; Carrió, J.G.; Dos Santos, D.R.; Da Silva, E.C.; Garcia-Quiroz, A.; Vargas, H. Soil characterisation using X-ray diffraction, photoacoustic spectroscopy and electron paramagnetic resonance. *Appl. Clay Sci.* **2002**, *21*, 303–311. [CrossRef]
65. Schmidt, R.L. Applications of photoacoustic spectroscopy to the study of soils and clay minerals. In *Advanced Chemical Methods for Soil and Clay Minerals Research*; Stucki, J.W., Banwart, W.L., Eds.; Springer: Dordrecht, Germany, 1980; pp. 451–465.
66. Bauer, A.; Hertzberg, O.; Kuderle, A.; Strobel, D.; Pleitez, M.A.; Mantele, W. IR-spectroscopy of skin in vivo: Optimal skin sites and properties for non-invasive glucose measurement by photoacoustic and photothermal spectroscopy. *J. Biophoton.* **2018**, *11*, e201600261. [CrossRef]
67. Brangule, A.; Skadins, I.; Reinis, A.; Gross, K.A.; Kroica, J. In vitro characterization perspectives using fourier transform infrared photoacoustic spectroscopy (FTIR-PAS) and diffuse reflectance infrared spectroscopy (DRIFT). *Key Eng. Mater.* **2017**, *758*, 273–277. [CrossRef]
68. Kizil, R.; Irudayaraj, J. Fourier transform infrared photoacoustic spectroscopy (FTIR-PAS). In *Encyclopedia of Biophysics*; Roberts, G.C.K., Ed.; Springer: Berlin/Heidelberg, Germany, 2013; pp. 840–844.
69. Michaelian, K.H.; Wen, Q. Photoacoustic infrared spectroscopy of solids. *J. Phys. Conf. Ser.* **2010**, *214*, 012004. [CrossRef]
70. Changwen, D.; Jianmin, Z.; Goyne, K.W. Organic and inorganic carbon in paddy soil as evaluated by mid-infrared photoacoustic spectroscopy. *PLoS ONE* **2012**, *7*, e43368. [CrossRef] [PubMed]
71. Doerr, S.H.; Thomas, A.D. The role of soil moisture in controlling water repellency: New evidence from forest soils in Portugal. *J. Hydrol.* **2000**, *231-232*, 134–147. [CrossRef]
72. Ma'Shum, M.; Tate, M.E.; Jones, G.P.; Oades, J.M. Extraction and characterization of water-repellent materials from Australian soils. *J. Soil Sci.* **1988**, *39*, 99–110. [CrossRef]
73. Du, C.; Ma, Z.; Zhou, J.; Goyne, K.W. Application of mid-infrared photoacoustic spectroscopy in monitoring carbonate content in soils. *Sens. Actuat. B* **2013**, *188*, 1167–1175. [CrossRef]
74. Ma, F.; Zeng, Y.; Du, C.; Shen, Y.; Ma, H.; Xu, S.; Zhou, J. Soil variability description using Fourier transform mid-infrared photoacoustic spectroscopy coupling with RGB method. *Catena* **2017**, *152*, 190–197. [CrossRef]
75. Du, C.; Zhou, J.; Liu, J. Identification of Chinese medicinal fungus Cordyceps sinensis by depth-profiling mid-infrared photoacoustic spectroscopy. *Spectrochim. Acta A Mol. Biomol. Spectrosc.* **2017**, *173*, 489–494. [CrossRef]
76. Ma, F.; Du, C.; Zhou, J. A self-adaptive model for the prediction of soil organic matter using mid-infrared photoacoustic spectroscopy. *Soil Sci. Soc. Am. J.* **2016**, *80*. [CrossRef]
77. Peltre, C.; Bruun, S.; Du, C.; Thomsen, I.K.; Jensen, L.S. Assessing soil constituents and labile soil organic carbon by mid-infrared photoacoustic spectroscopy. *Soil Biol. Biochem.* **2014**, *77*, 41–50. [CrossRef]
78. Du, C.; Goyne, K.W.; Miles, R.J.; Zhou, J. A 1915–2011 microscale record of soil organic matter under wheat cultivation using FTIR-PAS depth-profiling. *Agron. Sustain. Dev.* **2013**, *34*, 803–811. [CrossRef]
79. Huang, P.-M.; Wang, M.-K.; Chiu, C.-Y. Soil mineral–organic matter–microbe interactions: Impacts on biogeochemical processes and biodiversity in soils. *Pedobiologia* **2005**, *49*, 609–635. [CrossRef]
80. Du, C.; Zhou, G.; Wang, H.; Chen, X.; Zhou, J. Depth profiling of clay–xanthan complexes using step-scan mid-infrared photoacoustic spectroscopy. *J. Soils Sed.* **2010**, *10*, 855–862. [CrossRef]
81. Pasieczna-Patkowska, S.; Madej, J. Comparison of photoacoustic, diffuse reflectance, attenuated total reflectance and transmission infrared spectroscopy for the study of biochars. *Pol. J. Chem. Technol.* **2018**, *20*, 75–83. [CrossRef]
82. Sorokina, N.P.; Kozlov, D.N.; Kuznetsova, I.V. Assessment of the postagrogenic transformation of soddy-podzolic soils: Cartographic and analytic support. *Eurasian Soil Sci.* **2013**, *46*, 1007–1019. [CrossRef]
83. Travnikova, L.S.; Artem'eva, Z.S.; Sorokina, N.P. Distribution of the particle-size fractions in soddy-podzolic soils subjected to sheet erosion. *Eurasian Soil Sci.* **2010**, *43*, 459–467. [CrossRef]
84. Volkov, D.S.; Rogova, O.B.; Proskurnin, M.A.; Farkhodov, Y.R.; Markeeva, L.B. Thermal stability of organic matter of typical chernozems under different land uses. *Soil Tillage Res.* **2020**, *197*, 104500. [CrossRef]

85. Cherkassov, G.N.; Masyutenko, N.P.; Gostev, A.V.; Pykhtin, I.G.; Zdorovtsov, I.P.; Akimenko, A.S. Long-term field experiments on chernozemic soils of kursk region, Russia. In Proceedings of the Soil Organic Matter Dynamics in Long-Therm Field Experiments and their Modelling, Kursk, Russia, 14–17 September 2010; p. 35.
86. Kuznetsova, I.V. Changes in the physical status of the typical and leached chernozems of Kursk oblast within 40 years. *Eurasian Soil Sci.* **2013**, *46*, 393–400. [CrossRef]
87. Khaidapova, D.D.; Chestnova, V.V.; Shein, E.V.; Milanovskii, E.Y. Rheological properties of typical chernozems (Kursk oblast) under different land uses. *Eurasian Soil Sci.* **2016**, *49*, 890–897. [CrossRef]
88. McClelland, J.F.; Jones, R.W.; Bajic, S.J.; Griffiths, P.R. Photoacoustic spectroscopy. In *Handbook of Vibrational Spectroscopy*; Chalmers, J.M., Griffiths, P.R., Eds.; Wiley: Chichester, UK, 2006.
89. Michaelian, K.H. *Photoacoustic IR Spectroscopy: Instrumentation, Applications and Data Analysis*, 2nd ed.; Revised and Enlarged Edition Ed.; Wiley-VCH: Weinheim, Germany, 2010; p. 402.
90. Khaidapova, D.D.; Klyueva, V.V.; Skvortsova, E.B.; Abrosimov, K.N. Rheological properties and tomographically determined pore space of undisturbed samples of typical chernozems and soddy-podzolic soils. *Eurasian Soil Sci.* **2018**, *51*, 1191–1199. [CrossRef]
91. Chizhikova, N.; Varlamov, E.; Savich, V. Behavior of minerals in agro soddy podzolic soils resulted from different rates of organic fertilizers. *Dokuchaev Soil Bull.* **2014**, 91–110. [CrossRef]
92. Goncharov, V.D.; Moiseev, K.G. Dependence of the aggregate swelling parameters in soddy-podzolic soils on their properties. *Eurasian Soil Sci.* **2013**, *46*, 548–555. [CrossRef]
93. Gusarov, A.V.; Sharifullin, A.G.; Golosov, V.N. Contemporary trend in erosion of arable ordinary chernozems (Haplic Chernozems (Pachic)) within the Volga Upland (Saratov Oblast, Russia). *Eurasian Soil Sci.* **2018**, *51*, 1514–1532. [CrossRef]
94. Chendev, Y.G.; Khokhlova, O.S.; Alexandrovskiy, A.L. Agrogenic evolution of automorphic chernozems in the forest-steppe zone (Belgorod oblast). *Eurasian Soil Sci.* **2017**, *50*, 499–514. [CrossRef]
95. Mikhailova, E.A.; Post, C.J. Organic carbon stocks in the Russian Chernozem. *Eur. J. Soil Sci.* **2006**, *57*, 330–336. [CrossRef]
96. Schwanninger, M.; Rodrigues, J.C.; Fackler, K. A review of band assignments in near infrared spectra of wood and wood components. *J. Near Infrared Spectrosc.* **2011**, *19*, 287–308. [CrossRef]
97. Beć, K.B.; Futami, Y.; Wójcik, M.J.; Ozaki, Y. A spectroscopic and theoretical study in the near-infrared region of low concentration aliphatic alcohols. *Phys. Chem. Chem. Phys.* **2016**, *18*, 13666–13682. [CrossRef] [PubMed]
98. Krongtaew, C.; Messner, K.; Ters, T.; Fackler, K. Characterization of key parameters for biotechnological lignocellulose conversion assessed by FT-NIR spectroscopy. Part I: Qualitative analysis of pretreated straw. *BioResources* **2010**, *5*, 2063–2080.
99. Workman, J.; Weyer, L. *Practical Guide to Interpretive Near-Infrared Spectroscopy*; CRC Press: Boca Raton, USA, 2007.
100. Heaney, P.J.; Kronenberg, A.K.; Prewitt, C.T.; Gibbs, G.V. Chapter 4. Hydrogen speciation and chemical weakening of quartz. In *Silica*; De Gruyter: Berlin, Germany, 1994; pp. 123–176.
101. Russell, J.D.; Fraser, A.R. Infrared methods. In *Clay Mineralogy: Spectroscopic and Chemical Determinative Methods*; Wilson, M.J., Ed.; Springer: Dordrecht, The Netherlands, 1994; pp. 11–67.
102. Madejová, J.; Komadel, P. Baseline studies of the clay minerals society source clays: Infrared methods. *Clays Clay Miner.* **2001**, *49*, 410–432. [CrossRef]
103. Marchessault, R.H.; Liang, C.Y. Infrared spectra of crystalline polysaccharides. III. Mercerized cellulose. *J. Polym. Sci.* **1960**, *43*, 71–84. [CrossRef]
104. Hofmeister, A.M.; Bowey, J.E. Quantitative infrared spectra of hydrosilicates and related minerals. *Mon. Not. R. Astron. Soc.* **2006**, *367*, 577–591. [CrossRef]
105. Shinoda, K.; Aikawa, N. Absorption coefficients of overtone and combination modes of quartz. *Mineral. Mag.* **1994**, *58*, 601–606. [CrossRef]
106. Spitzer, W.G.; Kleinman, D.A. Infrared lattice bands of quartz. *Phys. Rev.* **1961**, *121*, 1324–1335. [CrossRef]
107. Calderón, F.J.; Reeves, J.B.; Collins, H.P.; Paul, E.A. Chemical differences in soil organic matter fractions determined by diffuse-reflectance mid-infrared spectroscopy. *Soil Sci. Soc. Am. J.* **2011**, *75*, 568–579. [CrossRef]
108. Changwen, D.; Jing, D.; Jianmin, Z.; Huoyan, W.; Xiaoqin, C. Characterization of greenhouse soil properties using mid-infrared photoacoustic spectroscopy. *Spectrosc. Lett.* **2011**, *44*, 359–368. [CrossRef]
109. Holman, H.-Y.N.; Wozei, E.; Lin, Z.; Comolli, L.R.; Ball, D.A.; Borglin, S.; Fields, M.W.; Hazen, T.C.; Downing, K.H. Real-time molecular monitoring of chemical environment in obligate anaerobes during oxygen adaptive response. *Proc. Natl. Acad. Sci. USA* **2009**, *106*, 12599–12604. [CrossRef] [PubMed]
110. Max, J.-J.; Chapados, C. Isotope effects in liquid water by infrared spectroscopy. III. H_2O and D_2O spectra from 6000 to 0 cm (-1). *J. Chem. Phys.* **2009**, *131*, 184505. [CrossRef] [PubMed]
111. Tan, C.Z. Optical interference in overtones and combination bands in α-quartz. *J. Phys. Chem. Solids* **2003**, *64*, 121–125. [CrossRef]
112. Hadži, D.; Pintar, M. The OH in-plane deformation and the C-O stretching frequencies in monomeric carboxylic acids and their association shifts. *Spectrochim. Acta* **1958**, *12*, 162–168. [CrossRef]
113. Asselin, M.; Sandorfy, C. Anharmonicity and hydrogen bonding. The in-plane OH bending and its combination with the OH stretching vibration. *Can. J. Chem.* **1971**, *49*, 1539–1544. [CrossRef]
114. Bock, J.; Su, G.-J. Interpretation of the infrared spectra of fused silica. *J. Am. Ceram. Soc.* **1970**, *53*, 69–73. [CrossRef]
115. Senesi, N.; D'Orazio, V.; Ricca, G. Humic acids in the first generation of EUROSOILS. *Geoderma* **2003**, *116*, 325–344. [CrossRef]

116. Koike, C.; Noguchi, R.; Chihara, H.; Suto, H.; Ohtaka, O.; Imai, Y.; Matsumoto, T.; Tsuchiyama, A. Infrared spectra of silica polymorphs and the conditions of their formation. *Astrophys. J.* **2013**, *778*, 60. [CrossRef]
117. Cavalli, M.; Gnappi, G.; Montenero, A.; Bersani, D.; Lottici, P.P.; Kaciulis, S.; Mattogno, G.; Fini, M. Hydroxy- and fluorapatite films on Ti alloy substrates: Sol-gel preparation and characterization. *J. Mater. Sci.* **2001**, *36*, 3253–3260. [CrossRef]
118. Lucas, S.; Tognonvi, M.T.; Gelet, J.-L.; Soro, J.; Rossignol, S. Interactions between silica sand and sodium silicate solution during consolidation process. *J. Non-Cryst. Solids* **2011**, *357*, 1310–1318. [CrossRef]
119. Bleken, B.T.; Mino, L.; Giordanino, F.; Beato, P.; Svelle, S.; Lillerud, K.P.; Bordiga, S. Probing the surface of nanosheet H-ZSM-5 with FTIR spectroscopy. *Phys. Chem. Chem. Phys.* **2013**, *15*, 13363–13370. [CrossRef]
120. De Benedetto, G.E.; Laviano, R.; Sabbatini, L.; Zambonin, P.G. Infrared spectroscopy in the mineralogical characterization of ancient pottery. *J. Cult. Herit.* **2002**, *3*, 177–186. [CrossRef]
121. Roeges, N.P.G. *A Guide to the Complete Interpretation of Infrared Spectral of Organic Structures*; Wiley: Chichester, UK, 1994.
122. Yu, H.-G.; Nyman, G. The infrared and Uv-visible spectra of polycyclic aromatic hydrocarbons containing (5, 7)-member ring defects: A theoretical study. *Astrophys. J.* **2012**, *751*, 3. [CrossRef]
123. Inoue, A.; Watanabe, T. Infrared spectra of interstratified illite/smectite from hydrothermally altered tuffs (Shinzan, Japan) and diagenetic bentonites (Kinnekulle, Sweden). *Clay Sci.* **1989**, *7*, 263–275. [CrossRef]
124. Noda, L.; Sensato, F.; Gonçalves, N. Titanyl sulphate, an inorganic polymer: Structural studies and vibrational assignment. *Química Nova* **2019**, *42*, 1112–1115. [CrossRef]
125. Workman, J. *The Handbook of Organic Compounds, Three-Volume Set: NIR, IR, R, and UV-Vis Spectra Featuring Polymers and Surfactants*; Elsevier Science: Amsterdam, The Netherlands, 2000.
126. Rothman, L.S. Infrared energy levels and intensities of carbon dioxide. Part 3. *Appl. Opt.* **1986**, *25*, 1795–1816. [CrossRef]
127. Lin-Vien, D.; Colthup, N.B.; Fateley, W.G.; Grasselli, J.G. *The Handbook of Infrared and Raman Characteristic Frequencies of Organic Molecules*; Elsevier Science: Amsterdam, The Netherlands, 1991.
128. Frost, R.L.; Vassallo, A.M. The dehydroxylation of the kaolinite clay minerals using infrared emission spectroscopy. *Clays Clay Miner.* **1996**, *44*, 635–651. [CrossRef]
129. Vempati, R.K.; Loeppert, R.H.; Sittertz-Bhatkar, H.; Burghardt, R.C. Infrared vibrations of hematite formed from aqueous- and dry-thermal incubation of si-containing ferrihydrite. *Clays Clay Miner.* **1990**, *38*, 294–298. [CrossRef]
130. Wenrich, M.L.; Christensen, P.R. Optical constants of minerals derived from emission spectroscopy: Application to quartz. *J. Geophys. Res. Solid Earth* **1996**, *101*, 15921–15931. [CrossRef]
131. Colthup, N.B.; Daly, L.H.; Wiberley, S.E. *Introduction to Infrared and Raman Spectroscopy*; Elsevier Science: Amsterdam, The Netherlands, 1990.
132. Chen, S.; Yin, X.; Wang, S.; Wu, J. Effects of organic material types on temporal changes in characteristics of humic acids extracted from a chernozem. *Sustainability* **2019**, *11*, 5683. [CrossRef]
133. Tatzber, M.; Mutsch, F.; Mentler, A.; Leitgeb, E.; Englisch, M.; Gerzabek, M.H. Determination of organic and inorganic carbon in forest soil samples by mid-infrared spectroscopy and partial least squares regression. *Appl. Spectrosc.* **2010**, *64*, 1167–1175. [CrossRef] [PubMed]
134. Sahba, N.; Rockett, T.J. Infrared absorption coefficients of silica glasses. *J. Am. Ceram. Soc.* **1992**, *75*, 209–212. [CrossRef]
135. Cummings, K.D.; Tanner, D.B. Far-infrared ordinary-ray optical constants of quartz. *J. Opt. Soc. Am.* **1980**, *70*, 123–126. [CrossRef]
136. Beder, E.C.; Bass, C.D.; Shackleford, W.L. Transmissivity and absorption of fused quartz between 0.22 μ and 3.5 μ from room temperature to 1500 °C. *Appl. Opt.* **1971**, *10*, 2263–2268. [CrossRef] [PubMed]
137. Bertaux, J.; Froehlich, F.; Ildefonse, P. Multicomponent analysis of FTIR spectra; quantification of amorphous and crystallized mineral phases in synthetic and natural sediments. *J. Sediment. Res.* **1998**, *68*, 440–447. [CrossRef]
138. Volkov, D.S.; Krivoshein, P.K.; Proskurnin, M.A. Detonation nanodiamonds: A comparison study by photoacoustic, diffuse reflectance, and attenuated total reflection FTIR spectroscopies. *Nanomaterials* **2020**, *10*, 2501. [CrossRef] [PubMed]
139. Spitsyn, B.V.; Davidson, J.L.; Gradoboev, M.N.; Galushko, T.B.; Serebryakova, N.V.; Karpukhina, T.A.; Kulakova, I.I.; Melnik, N.N. Inroad to modification of detonation nanodiamond. *Diam. Relat. Mater.* **2006**, *15*, 296–299. [CrossRef]
140. Park, Y.; Noda, I.; Jung, Y.M. Novel developments and applications of two-dimensional correlation spectroscopy. *J. Mol. Struct.* **2016**, *1124*, 11–28. [CrossRef]
141. Ma, F.; Chen, J.-b.; Wu, X.-X.; Zhou, Q.; Sun, S.-Q. Rapid discrimination of Panax notogeinseng of different grades by FT-IR and 2DCOS-IR. *J. Mol. Struct.* **2016**, *1124*, 131–137. [CrossRef]
142. Noda, I. Frontiers of two-dimensional correlation spectroscopy. Part 1. New concepts and noteworthy developments. *J. Mol. Struct.* **2014**, *1069*, 3–22. [CrossRef]
143. Noda, I. Frontiers of two-dimensional correlation spectroscopy. Part 2. Perturbation methods, fields of applications, and types of analytical probes. *J. Mol. Struct.* **2014**, *1069*, 23–49. [CrossRef]
144. Chen, W.; Qian, C.; Liu, X.-Y.; Yu, H.-Q. Two-dimensional correlation spectroscopic analysis on the interaction between humic acids and TiO2 nanoparticles. *Environ. Sci. Technol.* **2014**, *48*, 11119–11126. [CrossRef]
145. Ma, F.; Du, C.; Zhou, J.; Shen, Y. Optimized self-adaptive model for assessment of soil organic matter using fourier transform mid-infrared photoacoustic spectroscopy. *Chemom. Intellig. Lab. Syst.* **2017**, *171*, 9–15. [CrossRef]